Numerical simulation of the Fischer Tropsch synthesis in fixed bed reactors

Vogels, Dirk

Award date:
2018

Technische Universiteit
Eindhoven
University of Technology

Where innovation starts

Department of Chemical Engineering and Chemistry
Multiphase Reactors Group (SMR)
Het Kranenveld 14, 5612 AZ Eindhoven
P.O. Box 513, 5600 MB Eindhoven
The Netherlands

Author
D. Vogels

ID
0781870

Graduation committee
Prof. Dr. Ir. J.A.M. Kuipers
Dr. Ir. E.A.J.F. Peters
Dr. Ir. I.A.W. Filot
V. Chandra MSc

Date
November 8, 2017

Numerical Simulation of the Fischer Tropsch Synthesis in fixed bed reactors

Master's Thesis

Where innovation starts

Abstract

The Fischer Tropsch process can be a great contributor in the search for alternative clean energy. In this work numerical simulations are performed of the Fischer Tropsch Synthesis (FTS). The work consists of three main parts. First the selectivity models proposed by Vervloet et al. (α-correlation) and Filot et al. (micro kinetic model) are implemented in a diffusion reaction model and compared. Secondly, the model from Filot et al. is implemented in a one-dimensional tubular fixed bed reactor model. In the final part direct numerical simulation, applying the immersed boundary method, of the FTS in fixed bed reactors is investigated.

When the H_2 over CO ratio (syngas ratio) and temperature are varied, the models show big differences. The α-correlation shows a simple dependency, whereas the micro kinetic model shows that at different conditions, other reaction mechanisms should be taken into account. For the production of longer hydrocarbons, a Sabatier's optimum is found varying the temperature. Increasing the H_2/CO ratio will in all cases increase the H_2 consumption rate compared to the CO consumption rate. The consumption rate of H_2 and the selectivity towards longer hydrocarbons in general is lower using the micro kinetic model. This is also observed when the models are implemented in a particle model.

The particle model shows that intraparticle diffusion of the syngas causes undesired conditions. CO diffuses slower than H_2, causing an increase in the syngas ratio. This causes the reaction rate to go up and the selectivity to go down. This undesired effect can be prevented by lowering the surface concentrations.

In a one-dimensional tubular reactor model 135 simulations are performed. Variation of the catalyst particle diameter as well as the variation of the syngas ratio showed to have two condradicting effects on the product selectivity. Increase of total concentration in all cases showed to decrease the product selectivity. Temperature rise due to the exothermic reaction as well as variation of the inlet and wall temperature have shown to have the greatest effect on the product selectivity and space time yield. For variation of temperature, again a Sabatier's optimum is found.

As a proof of concept, the α-correlation is used to simulate the FTS using DNS. The reaction diffusion problem yielded the same results in the IBM as in the 1D particle model. The mass equations are coupled to the energy equations, as is proven by simulating the solutions from Aris and Weisz and Hicks. A big step towards creating a three dimensional model of the FTS has been set, the computation time needed for resolving the system has however proven to be too great. Some recommendation are given for improvement of the simulation time.

Technische Universiteit
Eindhoven
University of Technology

Where innovation starts

Table of contents

Title
Numerical Simulation of the Fischer Tropsch Synthesis in fixed bed reactors

1 Introduction

Due to the depletion of oil reserves, the search for alternative energy sources has been stimulated [1]. Additionally, in many cities worldwide air pollution, caused by engine and industrial emmissions, causes health problems [2]. This has increased the demand for clean energy. The Fischer Tropsch Synthesis (FTS) can be a great contributor for solving both problems. Via the FTS, synthesis gas (syngas, a mixture of CO and H_2) can be converted to long chain paraffins and 1-olefins. These long chain hydrocarbons can be hydrocracked and isomerized into liquid fuels [3, 4].

Syngas can be yielded from a variety of sources. Technologies, such as gasification, exist, in which organic waste, biomass or coal is converted to syngas [5]. Natural gas can be converted to syngas via reforming or partial oxidation [6]. The production of liquid fuels from biomass and waste is however less established and not considered economically feasible [7]. Processes in which coal or natural gas is converted into liquid fuels via the FTS have been present around the globe for a few decades already [8].

Especially increasing the capacity of the gas to liquids process (GTL), in which natural gas is converted to liquid fuels, recently has become of increased interest. One of the reasons for this is that GTL fuels burn cleaner, as the SO_2, CO and NO_x emissions are significantly lower compared to oil based fuels reducing the local pollution [9]. Furthermore, an abundance of natural gas is present and it is believed to be possible to reduce the well to wheel CO_2 emissions up to 15 % when using GTL fuels instead of oil based fuels [10].

Mainly two reactor types are used for the FTS, namely the slurry bubble column and the multitubular fixed bed reactor. Compared to the fixed bed reactor, the slurry bubble column has the advantage that smaller catalyst particles can be used, reducing the amount of catalyst needed, and better distribution of the heat generated by the highly exothermic reaction in the reactor is possible. The advantage of operating a fixed bed reactor is that the catalyst is more easily separated from the product and the catalyst is less sensitive to H_2S poisoning, as only the first layer of catalyst will be poisoned [11]. The heat management in this reactor type is more difficult, but potentially can be improved by using other packings, such as solid-foams [12, 13]. The focus in this work will lie on the fixed bed reactor.

1.1 Fischer Tropsch products

Once hydrocarbon chain growth is initiated, the chain can either propagate via insertion of a C_1 molecule, or terminate. The propagation probability α is defined as the rate of propagation over the rate of propagation and the rate of termination (1.1). This mechanism, which

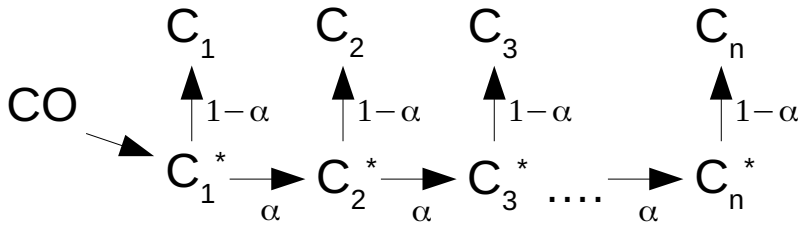

Figure 1.1: Simplified mechanism of the Fischer Tropsch Synthesis

is also described in figure 1.1, causes the FTS to produce a distribution of hydrocarbons with different carbon numbers. Of these products, hydrocarbon chains with carbon number greater than 5 (C_{5+}) are desired. Hydrocarbons with carbon numbers smaller than 5 are considered undesired side products.

$$\alpha = \frac{R_p}{R_p + R_t} \tag{1.1}$$

Probably the best known model to describe the selectivity towards the different products is the Anderson-Schulz-Flory (ASF) addition polymerization model. From this model a straight line is acquired when the logarithmic molar fraction of the products is plotted versus their carbon numbers [14]. Deviations to this ASF-plot are also commonly reported in literature [4, 15, 16]. Methane is often produced more and C_2 products, mainly ethylene, are often much less produced than is expected from the ASF-model. Another deviation is found for carbon numbers higher than approximately five to ten, where the slope of the line decreases and a higher production is found than predicted with the ASF-model. This is illustrated in figure 1.2.

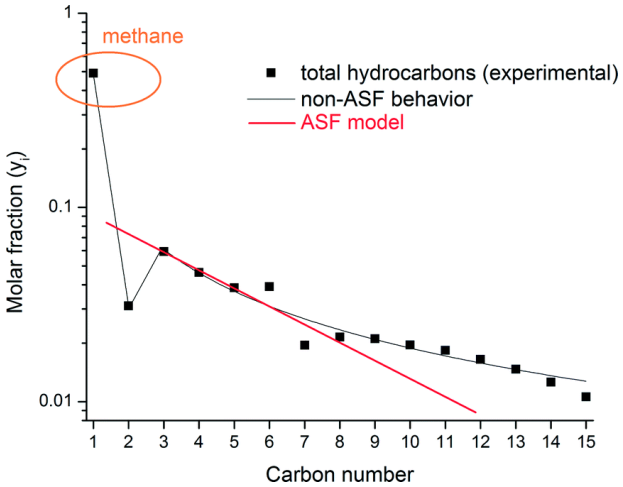

Figure 1.2: Example of an ASF-plot with experimental deviations. Adapted from Todic et al. [16]

Multiple explanations exist for the higher production of methane. In literature this is assigned to a higher termination rate for methane, intraparticle diffusion limitations of syngas or hotspots in the reactor. For the lower production of C_2 products it has to be noted that mainly less ethylene is produced. Readsorption and side reactions of the component are discussed in literature, but many arguments are made against these theories [4]. Only recently it is argued that the absence of substituents in ethylene causes a strong adsorption to the metal surface, decreasing the termination probability[17].

Considering the increased production of long chain paraffins, various explanations can be found in literature. It is often argued that long chain 1-olefins diffuse slowly through the catalyst particle, readsorb to the catalyst surface and start growing again before leaving the particle [18]. Others argue that both in the catalyst particle as in the reactor a variation is present in the H_2 over CO ratio, which can lead to the described deviation [19]. It is also stated that temperature gradients in the reactor, caused by the highly exothermic reaction, or concentration gradients due to difference in intraparticle diffusion speed, could also lead to a distribution that includes the decreasing slope found for long chain hydrocarbons [20].

1.2 Fischer Tropsch models

In literature different kinetics are suggested for the modeling of the FTS. The models vary from simplified kinetics based on the diffusion of hydrogen [21] to models that take into account the elementary reaction steps in a micro kinetic model based on statistical thermodynamics [22, 23]. When modeling a FTS fixed bed reactor, the simplified kinetics often miss certain details, which are necessary for gaining insights in the process. The implementation of micro kinetics in reactor models is however often difficult as data is required for many parameters.

Many kinetics independent of chain length describing the conversion of CO exist, using Langmuir-Hinshelwood type kinetics. Many of these kinetics are proposed in literature [24]. The kinetics proposed by Yates and Satterfield [25] are validated by other parties [26] and used in multiple reactor models. Langmuir-Hinshelwood type kinetics in which powers are fitted to experimental data and hence are a better fit to that data, are also reported [27]. These kinetics however cannot be derived from an assumed reaction mechanism.

The reactor models created are often simplified 1D models in which a variety of assumptions is made. Various ways are used to predict the product distribution and include the deviations to the ASF-model. For inclusion of the decreasing slope some use a two alpha model [28] and others introduce a distribution of propagation probabilities based on different conditions on both particle and reactor scale [20, 29]. The modeling of a pseudo homogeneous 2D-model is also reported in literature [30, 31].

Other models exist in which the reaction kinetics depend on the chain length of each specific hydrocarbon product [32, 33]. This model type is implemented in a reactor model as well [34]. In these kinetics the termination rate decreases exponentially as the chain length increases in order to model the increasing propagation probability for longer hydrocarbons. Kinetics based on the same principle of assigning reaction rates to the different products based on experimental results are made by numerous parties [35, 36].

Most of these models are well able to describe product distributions and conversions for a specific system. They, however, hardly provide a deeper understanding of the FTS kinetics, as they use reaction kinetics and selectivity models based on observed reaction rates and product distributions rather than intrinsic kinetics. Additionally, in the existing reactor models it is difficult to capture multi-dimensional effects such as hot spots, which can potentially influence the reaction.

1.3 Aim of the project

In this work the implementation of Fischer Tropsch kinetics in a fully resolved three dimensional model is investigated. To achieve this, the work is split into multiple main parts. First, two selectivity models will be compared. One often used selectivity model is proposed by Vervloet et al. [37]. In the derivation of the correlation for the propagation probability it is assumed that the propagation probability depends on the ratio of H_2 over CO (syngas ratio) according to a power law and that the difference between the activation ernergy of propagation and termination is constant. Further it is assumed that no CO_2 is produced.

Filot et al. have shown that for different temperatures the chain growth is influenced by different elementary steps, using a micro kinetic model based on density functional theory (DFT). The variation of syngas ratios is not taken into account in their work. As it is shown that very large ratios could be present in a catalyst particle [37], in this work it is investigated how the selectivity towards 50 hydrocarbon products is influenced by variation of the syngas ratio. The consumption rate of H_2 compared to the consumption rate of CO found via this model is also studied.

For further comparison the selectivity models are used to solve the diffusion reaction problem in a one-dimensional model. The selectivity models proposed by Todic et al. [33] and Visconti et al. [35] are not considered. In these models reaction rates for all products are fitted based on observed production rates in a reactor. In the reactor model possible causes for the deviations can be investigated. When the fitted reaction rates would be implemented in a multiscale model, the possibility exists that effects, such as concentration and temperature gradients, are accounted for twice.

Later the feasibility of implementing the micro kinetic model in a reactor model is discussed. In this part the micro kinetic model is implemented in a one-dimensional tubular reactor model, which is coupled to the particle model mentioned above. The reactor model is then used to investigate the influence of the temperature, catalyst diameter, inlet syngas ratio and inlet concentration on the space time yield (STY) of and selectivity towards C_{5+} products ($S_{C_{5+}}$).

In the final part of this work the implementation of the FTS in a three dimensional model is discussed. In this model, the fluid flow and heat and mass transfer equations are solved based on a computational fluid dynamics algorithm. Using this algorithm, exchange is a result of the imposed boundary conditions rather than of assumptions or correlations. This approach can lead to insights, which can improve correlations for bigger scale models. Performing simulations with such algorithms is commonly known as direct numerical simulation (DNS) [38]. In order to achieve this, the selectivity model proposed by Vervloet et al. is used, as its implementation in such a model is less extensive.

2 Comparison of models

To determine which selectivity model should be used in the fully resolved reactor model, it is important to compare the models discussed in the introduction. The first model that is investigated is the model proposed by Vervloet et al. [37]. The model consists of a correlation for the propagation probability. From the propagation probability the product distribution is then determined. This model will be referred to as the α-correlation. The model will be compared to the micro kinetic model developed by Filot et al. [39]. This model will be referred to as the micro kinetic model.

2.1 General comparison

In order to compare two selectivity models the product selectivity is determined for different temperatures and syngas ratios. The temperature is varied between 400 and 595 K in 40 steps. The syngas ratio is varied between 1 and 2^{15} in 16 steps. The pressure is set constant to 20 bar. If the models are to be implemented in particle or reactor models, it is also important to compare the consumption rate of H_2 over the consumption rate of CO. For both models the consumption rate of CO is based on the Langmuir-Hinshelwood kinetics proposed by Yates and Satterfield [25]. The consumption rate of CO will be discussed in more detail in section 2.2.1.

2.1.1 Methods and theory

Alpha correlation

Based on the definition of the propagation probability α and the reaction kinetics, Vervloet et al. proposed a correlation (2.1) that couples the propagation probability to the syngas ratio and the temperature [37]. This correlation is used to generate a product distribution. The product distribution is found by calculating the propagation probability for each grid cell. This probability is used to determine the mole fractions x of 50 hydrocarbon products via the ASF model given in equation (2.2), in which n is the carbon number and α is the propagation probability.

$$\alpha = \frac{1}{1 + k_\alpha \left(\frac{C_{H_2}}{C_{CO}}\right)^B \exp\left(\frac{\Delta E_\alpha}{R}\left(\frac{1}{498.15} - \frac{1}{T}\right)\right)} \tag{2.1}$$

Here ΔE_α is the difference in activation energy for the propagation and the termination step, R is the gas constant, T the temperature and k_α and B are fitting parameters. Of these parameters k_α represents the difference between the propagation and termination rate.

$$x_n = (1-\alpha)\alpha^{n-1} \tag{2.2}$$

For the reaction term of H_2 two limiting cases are present: 1. α = 0 and 2. α = 1. For case 1 it is obvious that the reaction term of H_2 is equal to three times the reaction term of CO, since the production of CO_2 is not included in this model. For case two this term will be equal two times the reaction term of CO. It can be reasoned that this results in a linear dependency of $r_{\mathrm{H_2}}$ on α as shown in equation (2.3).

$$-R_{H_2} = (3-\alpha)\,(-R_{CO}) \tag{2.3}$$

Micro kinetics

The software package MKMCXX is used for the generation of the micro kinetic data. Details on the used DFT calculations and the microkinetic simulations can be found in the work of Filot et al. [17, 39, 40, 41]. The program returns selectivities in mol/mol towards both 1-olefins as paraffins up to C_{50}. Although the possibility exists that 1-olefins readsorp and react to longer chains as discussed in section 1.1, this is outside the scope of this work. Therefore a Python script is used to extract the selectivities and add up the 1-olefins and paraffins of the same length.

In contrast to other FTS selectivity models, the removal of oxygen from the catalytic surface is taken into account. This means that the production of CO_2 is included as well. Logically the consumption of CO per hydrocarbon is equal to the carbon number n. Part of the consumption of H_2 will be determined by the amount of oxygen removed via the production of H_2O. Further consumption is dependent on the product distribution. Considering all products to be paraffins, for every mole of produced hydrocarbon with cabon number n, $n+1$ mole H_2 will be consumed. The consumption rate of H_2 compared to the consumption rate of CO can then be found via equation (2.4).

$$R_{H_2} = \left[\sum_{n=1}^{50}\left(x_n + {}^{1}\!/_{n}\right) + x_{H_2O}\right] R_{CO} \tag{2.4}$$

With x_n the selectivity towards paraffins with carbon number n in $mol_n/mol_{product}$.

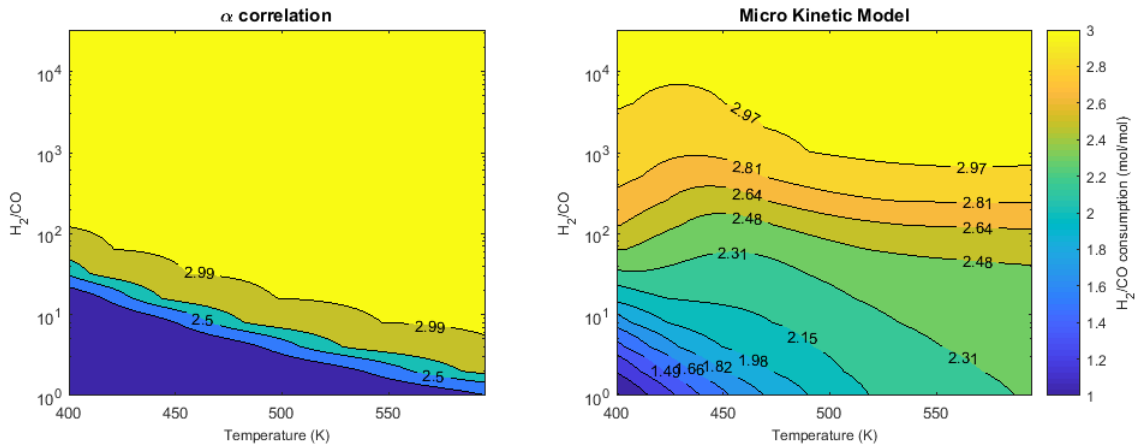

Figure 2.1: The consumption rate of H_2 over the consumption rate of CO for the α-correlation (left) and the micro kinetic model (right)

2.1.2 Comparison of model properties

Syngas consumption ratio

In figure 2.1 the consumption of H_2 compared to the consumption of CO is shown for the micro kinetic model and the α-correlation selectivity models respectivily. For the α-correlation the H_2 consumption shows the clear shape that is expected from equations (2.1) and (2.3). It can be seen that the consumption ratio varies between 2 and 3. Furthermore it can be seen that a higher temperature increases the consumption rate. A higher temperature will according to the model result in a lower propagation probability and thus a higher consumption of H_2. The same holds for an increase of syngas ratio. For this variable it can be seen that slightly increasing the ratio will rapidly increase the consumption ratio towards the upper limit of 3. For 490 K, a typical temperature for the FTS, this limit is already reached for a syngas ratio of approximately 13.

The micro kinetic model shows different consumption ratios compared to the α-correlation. Two reasons exist for these differences. The first reason is that the production of CO_2 is taken into account in the micro kinetic model. This allows the consumption ratio to go to a lower limit of 1 instead of 2. The second big difference between the models is that in the micro kinetic model many elementary reaction steps are taken into account. For the determination of the α-correlation, constant differences between the termination and propagation rate are assumed as well as a constant difference in activation energies between the propagation and the termination limiting reaction step. Earlier work showed however that the degree of chain growth control can vary for each elementary reaction step, based on reaction conditions [39].

Even though hydrogenation in some cases leads to a higher propagation probability, the addition of hydrogen for all the investigated temperatures increases the consumption ratio. When the ratio increases from 1 to 2, chain growth is indeed stimulated, as the production of CO_2 decreases. When the syngas ratio increases further, the increase of H_2 consumption is probably caused be the decrease in the propagation probability.

Product distribution

Another way to compare the two selectivity models is by comparing the selectivity towards C_{5+} products. The results of this comparison can be seen in figure 2.2. The α-correlation shows similar, but inverted, trends for the product selectivity as for the H_2/CO consumption. Since both the consumption ratio and the product selectivity solely depends on the propagation probability, this trend is expected.

The micro kinetic model does not only show big differences for extreme conditions, but also for typical reaction conditions of 490 K and a H_2:CO ratio of 2:1. An optimum can be found, which most likely can be addressed to Sabatier's principle as described by Filot et al. It can be seen that for low and high temperatures almost no C_{5+} product is created and at typical Fischer Tropsch temperatures the selectivity is highest.

Looking at figure 2.2 (c) it can be seen that the production of shorter hydrocarbons is not the only cause for lowering of the C_{5+} selectivity. Especially for low temperatures and low syngas ratios it should be noted that the sum of all hydrocarbons will not be unity. This is caused by the production of CO_2, which is highest for these conditions. The production of CO_2 is also seen at slightly higher temperatures for low syngas ratios. This causes the optimum seen in figure 2.2b. The micro kinetic model contradicts the assumption that the production of CO_2 can be neglected, made in the derivation of the α-correlation.

A big difference between the models is not only found in their trends, but also in the values of the selectivity towards C_{5+} products. At maximum the micro kinetic model finds a selectivity of 0.81 $kg_{C_{5+}}/kg_{product}$. The maximum selectivity found via the α-correlation is 1.0 $kg_{C_{5+}}/kg_{product}$. For a typical situation of the FTS of 490 K and a syngas ratio of 2 the micro kinetics model finds a selectivity of 0.77 $kg_{C_{5+}}/kg_{product}$. For this situation the selectivity found via the α-correlation is 0.98 $kg_{C5+}/kg_{product}$.

The differences between the models can best be discussed looking at how they are constructed. The α-correlation is based on the assumption that the determining steps for propagation and termination are the same for all the conditions. The correlation is then fitted to experimental data for determination of the parameters. The micro kinetic model however is much more extensive. It takes into account that the propagation and termination are in different conditions determined by one or more different reaction steps, based on statistical thermodynamics.

The micro kinetics model is verified on the basis of the reaction orders, the apparent activation energy, the methane selectivity and the chain-growth probability. Such kinetic parameters are the result of many detailed experiments at a relatively broad range of experimental conditions. In contrast, the alpha-correlation model is fitted to observed product selectivities resulting from a few carefully constructed experiments. Whereas the former has decent accuracy for a broad range of conditions, the latter has excellent accuracy for a smaller range of bigger scale experimental conditions.

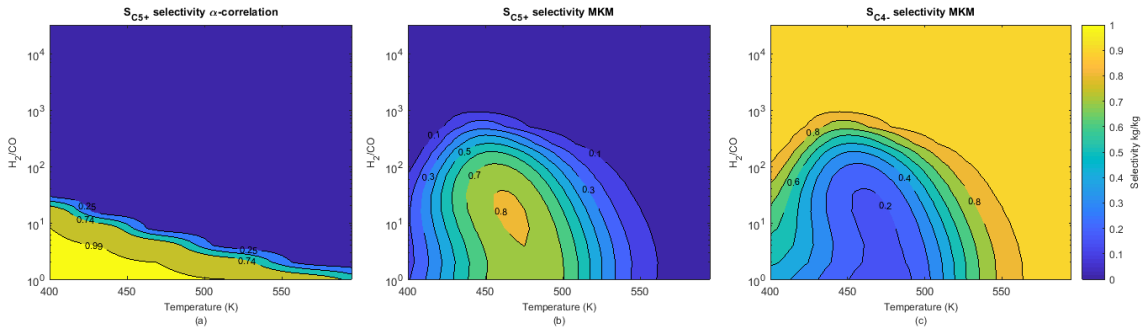

Figure 2.2: The selectivity towards C_{5+} hydrocarbons in $kg_{C_{5+}}/kg_{product}$ for (a) the α-correlation and (b) the micro kinetic model for a range of H_2/CO ratios and temperatures. (c) the selectivity towards CO_2 according to the micro kinetic model in mol/mol

2.2 Diffusion reaction in a spherical catalyst

2.2.1 Methods

For both selectivity models the reaction diffusion problem in a spherical particle is solved. A particle diameter of 3 mm is used. The surface concentration of H_2 and CO are set to be constant at 50 mol/m^3 and 25 mol/m^3 respectively. The temperature is assumed to be constant over the catalyst diameter. The inclusion of an energy balance is still described in this section, as it will be used in section 3.1 and to see if assuming an isothermal system is valid. The used parameters are given in table 2.1.

Numerical methods

In the particle model both the energy and the mass equation are solved using spherical coordinates. The governing equations are given by equation (2.5) and (2.6). It is assumed that the diffusion constant and the thermal conductivity are constant. The equations are solved using an implicit central differencing scheme.

$$\frac{\partial C_i}{\partial t} = D_i^{eff} \frac{1}{r^2} \left[\frac{\partial}{\partial r} \left(r^2 \frac{\partial C_i}{\partial r} \right) \right] + (-R_i) \tag{2.5}$$

$$\rho_s C_p \frac{\partial T}{\partial t} = k \frac{1}{r^2} \left[\frac{\partial}{\partial r} \left(r^2 \frac{\partial T}{\partial r} \right) \right] + (-R_i)\, \Delta H_r \tag{2.6}$$

In the governing equations C_i represents the concentration of species i, R_i the reaction rate of species i, ρ_s the solid density, C_p the catalyst specific heat capacity, k the thermal conductivity and r the particle radius. The effective diffusion coefficient D_i^{eff} is given in equation (2.7)

$$D_i^{eff} = \frac{\varepsilon_{TP}}{\tau_{TP}} D_i \tag{2.7}$$

With D_i the diffusion coefficient of specie i, ε_{TP} the porosity and τ_{TP} the tortuosity of the catalyst particle. As this section is only for the comparison of the kinetics, the effective diffusivity will be assumed to be equal to the diffusivity. In section 3.1 the obstruction in the catalyst pores will be taken into account.

For the surface of the particle Dirichlet boundary conditions are used, i.e. the surface concentration is set to be constant. For the center of the particle Neumann boundaries are used. Here the flux is forced to be zero.

Kinetics

Yates and Satterfield introduced an expression for Langmuir-Hinshelwood (LH) type kinetics for the Fischer Tropsch reaction considering that CO is present on the catalyst surface [25]. They have fitted the expression given by equation (2.8) for a few temperatures. In later work the parameters are fitted in an Arrhenius expression [26]. The expressions for the reaction parameters are given by equation (2.9) and (2.10).

$$-R_{CO} = \frac{a \cdot p_{H_2} p_{CO}}{(1 + b \cdot p_{CO})^2} \rho_s \tag{2.8}$$

$$a = 8.8533 \cdot 10^{-3} \exp\left[4494.41 \left(\frac{1}{493.15} - \frac{1}{T}\right)\right] \tag{2.9}$$

$$b = 2.226 \exp\left[-8236 \left(\frac{1}{493.15} - \frac{1}{T}\right)\right] \tag{2.10}$$

Physical properties

Literature describes the condensation of long chain hydrocarbons inside catalyst pores. This will cause H_2 and CO to diffuse at different rates. It is shown in literature that it takes 9 to 13 days, depending on operating conditions, before the pores in a catalyst particle are completely filled up with liquid hydrocarbons [42, 43]. As the steady state operation is the point of interest and because it is too computationally expensive to generate data equivalent to 13 days of real time in the DNS code, it is assumed that the pores are filled with liquid hydrocarbons from the start of the calculations.

Measurements are reported of H_2 and CO diffusion in liquid mixtures of hydrocarbons with carbon numbers greater than 28 at various temperatures. It is assumed that the diffusivities follow an Arrhenius type temperature dependency as given by equation (2.11) [44].

$$D_i = D_i^0 \exp\left(\frac{\Delta E_{D,i}}{RT}\right) \tag{2.11}$$

As the reagents are dissolved in liquid when inside the catalyst particle, the partial pressures are found by multiplying the concentration with Henry's coefficient H_i according to Henry's law:

$$p_i = H_i C_i \tag{2.12}$$

It should be noted that in the current discretization scheme it is assumed that the diffusion coefficient is a constant. For resolving non-isothermal systems, the diffusion coefficient inside the catalyst particle is therefor set to be an estimated constant based on equation (2.11). The temperature used to do this is either the surface temperature or the inlet temperature, depending on the system that is to be solved.

Post processing

For both the investigated selectivity models the product distribution is to be calculated when steady state is reached. For each grid cell this is done as is described in section 2.1.2. After the distributions are found, the mol fractions of the products are all multiplied with the volume of the grid cell V_{GC}, which is determined via equation (2.13), and the reaction rate in the grid cell found via equation (2.8). After giving each distribution its weight, the distributions are summed and normalized according to equation (2.14).

$$V_{GC,i} = \frac{4}{3}\pi\left(i\frac{r_p}{N_{GC}}\right)^3 - \sum_{j=0}^{i-1} V_{GC,j} \tag{2.13}$$

$$x_n = \frac{\sum_{i=1}^{nPGC} x_{n,i} R_{CO,i} V_{GC,i}}{\sum_{i=1}^{nPGC} R_{CO,i} V_{GC,i}} \tag{2.14}$$

In the equations above $nPGC$ stands for the amount of grid cells used over the radius of the catalyst particle. S_n is the selectivity towards products with carbon number n and is found as described in section 2.1.2.

The product selectivity is determined in units of $kg_{C5+product}/kg_{product}$. In order to find the selectivity, the mole fractions are first converted to weight fractions. After this is done, the weight fractions of C_{5+} products is summed to acquire the selectivity (2.15). Other papers suggest calculating the product selectivity by subtracting the weight fraction of the first four components from one. As in the micro kinetic model CO_2 is included, this method will not give the valid selectivity.

$$S_{C_{5+}} = \frac{\sum_{n=5}^{50} x_n\,(14n+2)}{\sum_{n=1}^{50} x_n\,(14n+2)} \tag{2.15}$$

Table 2.1: Parameter values isothermal diffusion reaction in a sperical particle

Symbol	Description	Value	Motivation
ρ_s	Solid density	1000 $kg\ m^{-3}$	assumed
D^0_{CO}	CO diffusion coefficient in product wax	5.584·10^{-7} $m^2\ s^{-1}$	[44]
$D^0_{H_2}$	H_2 diffusion coefficient in product wax	1.085·10^{-6} $m^2\ s^{-1}$	[44]
$E_{D,CO}$	CO diffusion activational energy	14.85·10^3 $J\ mol^{-1}$	[44]
E_{D,H_2}	H_2 diffusion activation energy	13.51·10^3 $J\ mol^{-1}$	[44]
H_{CO}	Henry coefficient CO	0.21 $bar\ m^3\ mol^{-1}$	[45]
H_{H_2}	Henry coefficient H_2	0.27 $bar\ m^3\ mol^{-1}$	[45]
nPGC	Grid cells over the particle radius	20	set
dt	Time step size	0.05 s	set
T	Temperature	490 K	set
C_{s,H_2}	Surface concentration H_2	50 $m^3\ mol^{-1}$	set
$C_{s,CO}$	Surface concentration CO	25 $m^3\ mol^{-1}$	set
r_p	Particle radius	1.5 $\cdot\ 10^{-3}$ m	set

Another quantity that is calculated is the effectiveness factor η. The effectiveness factor can be found by dividing the actual CO consumption rate in the particle by the amount of CO that would be consumed if the surface concentration was present in the whole particle. This leads to equation (2.16). In this equation $R_{CO,0}$ is the reaction rate at the surface of the catalyst.

$$\eta = \frac{\iiint_{V_{cat}} R_{CO}(V) dV}{R_{CO,0} V_{cat}} \tag{2.16}$$

Implementation of the micro kinetic model

The selectivity models have to be used during the calculations, as the consumption of hydrogen depends on the selectivity towards the various products that are made. For the α-model this calculation is discussed in section 2.1.1. For this selectivity model equations (2.1) and (2.3) are solved in each grid cell for every time step to determine the consumption of H_2.

The implementation of the micro kinetic model requires communication between a variety of programs. Two ways of implementation are compared. In the first method, the micro kinetic model is solved for each grid cell for every time step. In the second method, a spline is created based on 16 data points from which the consumption of H_2 is interpolated.

In a grid cell first the temperature and the syngas ratio are rounded to integers. The found values are then used to create a string. To save computational time, the Matlab 'exist' function is used to check if a folder with the name of the string already exists. If this is the case, the data in the folder is imported and used to calculate the reaction rate of H_2 according to equation (2.4).

If the folder does not yet exist, this means that the data to determine R_{H2} is to be generated. To do this, first a folder is created with the string as name. To this folder the input file for

MKMCXX is copied and MKMCXX is run. A Python script is then used to get the selectivities as described in section 2.1.2. These selectivities are used to calculate the reaction rate of H_2. To save computational time, the consumption ratio is assumed to be 3.0 for syngas ratios greater than 8000.

As one calculation for one temperature and one syngas ratio with the micro kinetic model takes approximately one and half a minute, computational time can greatly be reduced if data could be interpolated from a set of data points rather than be calculated for every specific point. To this end a spline is created using 16 syngas ratios. The spline is created using Matlab's spline function. The ratios used to make the spline are defined by the set $\{x = 2^i | i \in \mathbb{Z} \cap 0 \leq i \leq 15\}$.

2.2.2 Results

As discussed in the previous section, it is investigated whether spline interpolation can be used for the implementation of the micro kinetic model. The H_2 concentration profiles for both implementation methods and the relative difference between them are given in table A.1. The difference is the smallest near the surface of the particle, where it is only $6 * 10^{-3}\%$. The error slowly becomes bigger going towards the center of the particle up to 0.76 %. Because the deviation is less than 0.76 % and the computational time is greatly reduced using spline interpolation, for the generation of further data spline interpolation will be used for the implementation of the micro kinetic model.

The dimensionless concentrations of H_2 and CO and the dimensionless reaction rate are given in figure 2.3 for both models. The dimensionless quantities match well with the shapes of other particle models reported in literature [29, 37]. The figure clearly shows a rapid decrease in CO concentration going from the particle surface to the particle centre. The same is the case for H_2. The concentration of H_2 decreases however less fast and stops decreasing from the point where the CO is vanished.

The observed profiles are all as expected. Due to the difference in diffusion rates of H_2 and CO it is expected that in the centre of the particle more H_2 is present than CO. CO will simply react away fast in the presence of an excess of H_2. Lowering of the CO concentration will initially cause the reaction rate to increase, due to its negative order. At a certain point the concentration is lower and the reaction order approaches one. Here the reaction rate goes towards zero.

The difference between the two models is that in the micro kinetic model relatively less H_2 is consumed. This matches the trends observed in section 2.1.2. Here it is clearly shown that the consumption of H_2 much faster reaches the upper limit of three for an increasing syngas ratio in the α-correlation model than in the micro kinetic model.

The found effectiveness factors are 0.94 for the α-correlation and 1.0 for the micro kinetic model. The higher concentration of H_2 found via the micro kinetic model can be translated to the higher reaction rate in the catalyst particle. The higher reaction rate can again be translated to a higher effectiveness factor. An effectiveness factor of 1.0 is found when intraparticle diffusion is infinitely fast. In the case of a negative order it is however possible to acquire effectiveness factors greater than one. This allows the high effectiveness factors to be achieved even tough the intraparticle diffusion is slow.

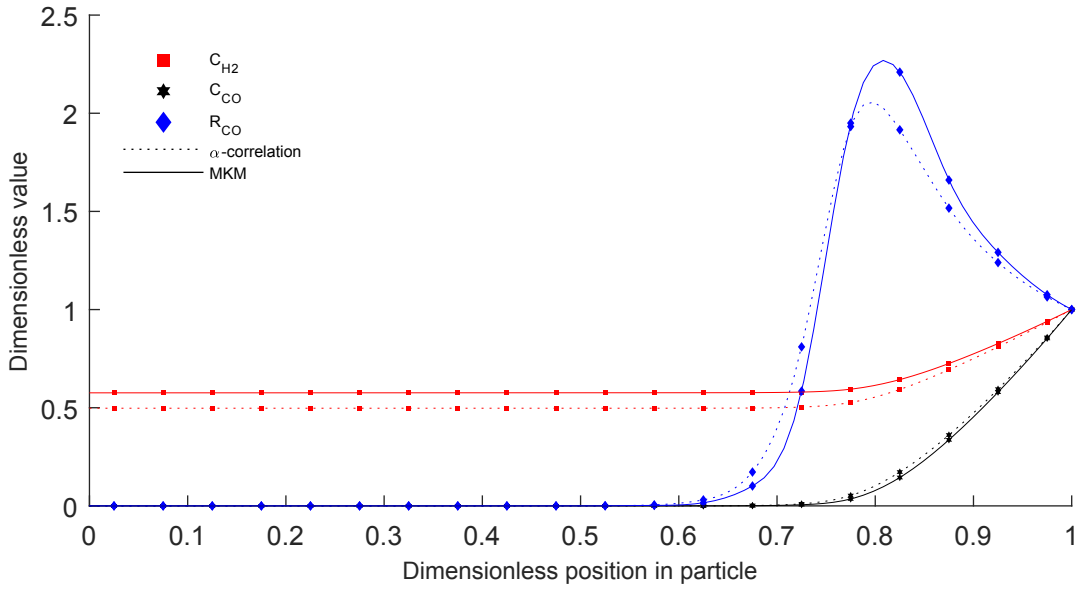

Figure 2.3: Dimensionless profiles over the dimensionless particle length, with 0 the particle center and 1 the particle surface. T = 490 K, $d_p = 3\ mm$, P = 20 bar, $C_{\mathrm{H_2},0} = 50\ mol\ m^{-3}$, $C_{\mathrm{CO},0} = 25\ mol\ m^{-3}$. The dotted line represents the results found via the α-correlation and the full line the results found via the micro kinetic model

When the selectivities towards the first 50 hydrocarbons are investigated, the differences between the two selectivity models are bigger. The selectivities can be found in figure 2.4. To see the effect of intra particle diffusion, the product distribution corresponding to the surface conditions is also shown.

The selectivity towards C_{5+} products for the micro kinetic model is 0.53 and for the α-correlation 0.83 kg/kg. In section 2.1.2 a similar difference between the models is found and discussed. For the α-correlation the selectivity decreases with an exponentially decreasing slope with increasing carbon numbers. Concentration gradients caused by intraparticle diffusion are given as a possible cause for the decreasing slope often observed in ASF-plots by the creators of the α-correlation [20].

This decreasing slope is however not observed when the particle model is solved using the micro kinetic model. The use of this model resulted in an ASF-plot in which the C_1 and C_2 deviations are present, but the decreasing slope is not. The decreasing slope is often assigned to the readsorption of long chain 1-olefins. Not modelling this is readsorption could be the cause for missing this deviation. The decreasing slope is according to this model not likely caused by concentration gradients. Inclusion of readsorption would also increase the product selectivity.

Compared to the product distribution found for the surface conditions, the product distribution found for the particle model, in which the micro kinetic model is used, shows many simularities. A notable difference is found looking at the selectivity towards C_1 and C_2 products. For these products much higher selectivities are found when the particle model is solved. The selectivity towards methane increased the most from 0.010 mol/mol at the surface to 0.074 for the whole catalyst particle. This indicates that the increasing syngas ratio in the

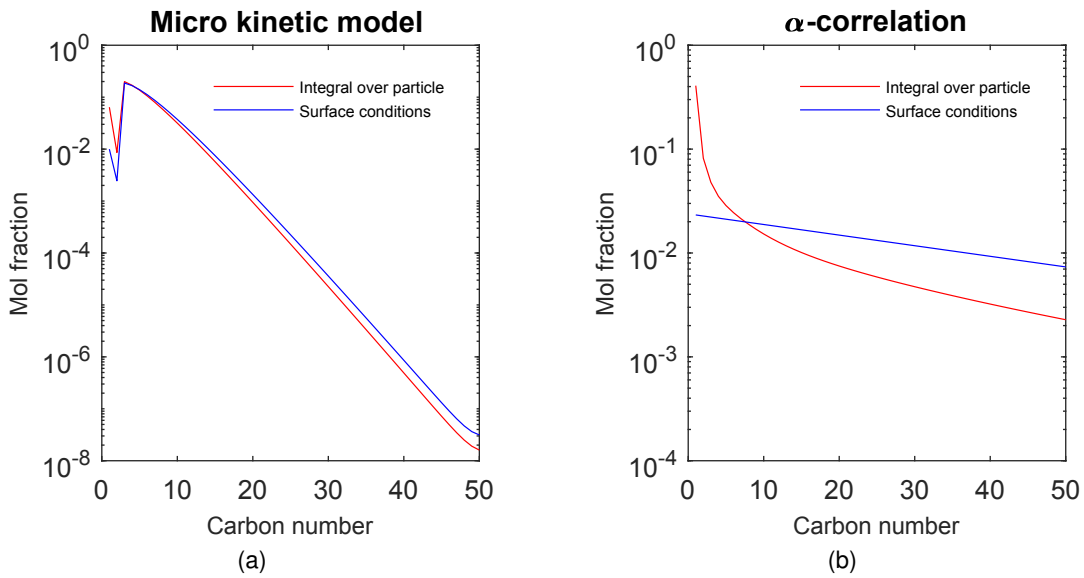

Figure 2.4: Selectivities towards 50 hydrocarbons found via a volume integral over the particle and for the surface conditions according to (a) the micro kinetic model and (b) the α-correlation. T = 490 K, $d_p = 3\ mm$, P = 20 bar, $C_{\mathrm{H_2},in} = 50\ mol\ m^{-3}$, $C_{\mathrm{CO},in} = 25\ mol\ m^{-3}$.

catalyst particle could be partly the cause of the increased methane production, which is often described.

For both models it is found that the selectivity towards C_{5+} products is lower for the whole catalyst particle than for the surface conditions. The selectivities at the surface are 0.77 and 0.98 for the micro kinetic model and the α-correlation respecitively. The difference between these values are big. They however do show the similar trend where the C_{5+} selectivity corresponding to the bulk conditions is higher than the selectivity corresponding to the conditions inside the catalyst particle.

As mentioned above, it appears that the intraparticle diffusion differences between H_2 and CO cause a lower product selectivity. The negative order of CO enhances this effect even further. If the concentration of CO is decreased, the reaction rate goes up, while the product selectivity goes down. To investigate this effect, an extra simulation is performed.

Equation (2.8) shows that the order of CO varies between -1 and 1, depending on its concentration. If the concentration approaches zero, the order will be 1 and when it approaches infinity, the order will be -1. A simulation is performed using the micro kinetic model where the concentration is lowered, to further investigate this effect. The results can be seen in figure 2.5.

The profiles shown in figure 2.5 confirm the influence of the concentration on the reaction order of CO. In this case the reaction rate lowers as the concentration of CO lowers. Figure 2.4 shows that this is not the case for a higher surface concentration. The selectivity towards C_5 products is also higher in this case. It is 0.77 compared to 0.53 for the higher concentration.

For the model using the α-correlation a non-isothermal run is done as well. Here a maximum temperature rise of 0.66 K is found. It is in this case hence justified to assume that the system is isothermal.

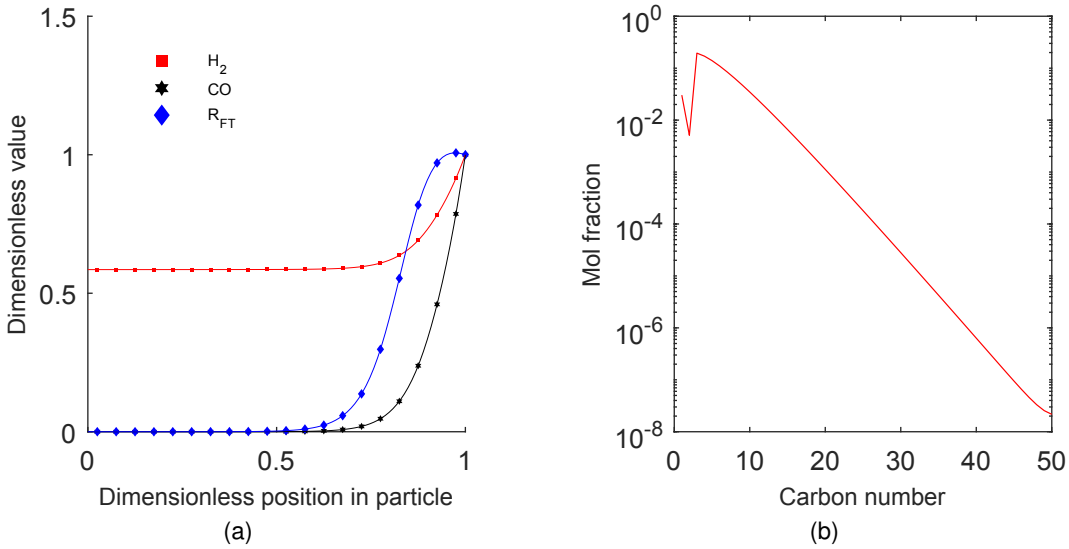

Figure 2.5: (a) The concentration and reaction profiles and (b) the product distribution according to the micro kinetic model for a lower concentration. T = 490 K, $d_p = 3\ mm$, P = 20 bar, $C_{\mathrm{H_2},in} = 10\ mol\ m^{-3}$, $C_{\mathrm{CO},in} = 5\ mol\ m^{-3}$.

A point of notice in this model is the usage of Fick's diffusion. Fick's law of diffusion holds when one or two components are present in the system. Once more species are added, interaction between species can possibly influence the diffusion rates. In this case produced longer hydrocarbon chains would condensate and be pushed out of the particle, due to pressure build up. This moving of hydrocarbons towards the surface of the particle could potentially influence the diffusion rates of the syngas towards the center of the particle [46].

3 1D reactor model

3.1 Methods

3.1.1 Numerical methods

A tubular reactor model is made that is coupled to the particle model described in the previous chapter. A total variation diminishing scheme with upwind deferred correction is used to solve the mass and energy equation as given by equations (3.1) and (3.2). It is assumed that a flat flow profile is present. Further the axial dispersion is neglected and external mass transfer is considered fast compared to intraparticle diffusion. This allows the concentration or temperature to be set as the constant surface concentration for the particle model in each grid cell.

$$\frac{\partial C_i}{\partial t} = -v_z \frac{\partial C_i}{\partial z} - s_M \tag{3.1}$$

$$\rho C_p \left[\frac{\partial T}{\partial t} + v_z \frac{\partial T}{\partial z} \right] = U a_R \left(T - T_w \right) - s_E \tag{3.2}$$

$$s_M = \left(1 - \varepsilon_b \right) a_p D^{eff} \frac{\partial c_i}{\partial r} |_{r=r_p} \tag{3.3}$$

$$s_E = \left(1 - \varepsilon_b \right) a_p k \frac{\partial T}{\partial r} |_{r=r_p} \tag{3.4}$$

In equation (3.2) a term can be seen for heat exchange with the wall. In this term U is the wall to bed heat transfer coefficient, a_R the specific surface area of the wall for one grid cell, and T_w the constant wall temperature. The coupling between the fluid phase is found by solving the surface integral of the flux from the fluid phase to the solid phase. This is for both equations the source term s. In this term, given by equations (3.3) and (3.4), ε_b is the bed porosity and a_p the specific surface area of a particle. v_z is the velocity in the axial direction and is assumed to be constant and equal to the inlet velocity.

Table 3.1: Investigated variables

Quantity	Value range	Amount of values
Inlet temperature	393.15 - 593.15 K	5
Inlet concentration H_2	10 - 150 mol m^{-3}	3
Inlet syngas ratio	1 - 3	3
Catalyst diameter	0.5 - 5 mm	3

3.1.2 System properties

The particle model discussed in section 2.2 is coupled to a 1-D tubular reactor model. The consumption of H_2 will be based on the micro kinetic model discussed in section 2.1.1. The model will not be used to determine the optimal operating conditions. The validity of the model is tested by observing whether variation of inlet temperature, inlet syngas ratio, catalyst particle diameter and inlet concentration fit the expected trends. The used parameters are given in table 3.1.

The wall temperature is set constant and equal to the inlet temperature. The bed to wall heat transfer coefficient is set to 0.02 $W\ m^{-2}\ K^{-1}$. The reactor length is set to 1 m and its diameter to 5 cm. For solving of the equations 100 grid cells are used over the axial direction of the reactor and the time step size is set to 0.1 s. The physical properties of the reactor are given in table 3.2.

3.1.3 Product selectivity

The quantities that are tested are the selectivity and space time yield towards C_{5+} products. The selectivity is found via equation (2.15). The determination of the mole fractions of the various products should however be adapted now that a tubular reactor model is solved. Integrating over the reactor length leads to equation (3.5). In this equation $nTGC$ is the amount of grid cells used over the axial direction of the reactor. The properties of the catalyst particles are equal to those stated in table 2.1.

Table 3.2: System parameters

Symbol	Description	Value
Cp_F	Fluid specific heat	1 $kJ\ kg^{-1}\ K^{-1}$
ϵ_b	Solid fraction	0.4
ρ_F	Fluid density	5 kg m^{-3}
U	Bed to wall heat transfer coefficient	0.02 W $m^{-2}\ K^{-1}$
$\frac{\epsilon_{TP}}{\tau_{TP}}$	Obstruction factor	0.2
k_s	Solid heat transfer coefficient	0.5 W $m^{-2}\ K^{-1}$
$(-\Delta H_r)$	Reaction enthalpy	-165 kJ mol_{CO}^{-1}
d_R	Reactor diameter	5 cm
L_R	Reactor length	1 m
Cp_s	Solid specific heat	10 J $kg^{-1}\ K^{-1}$

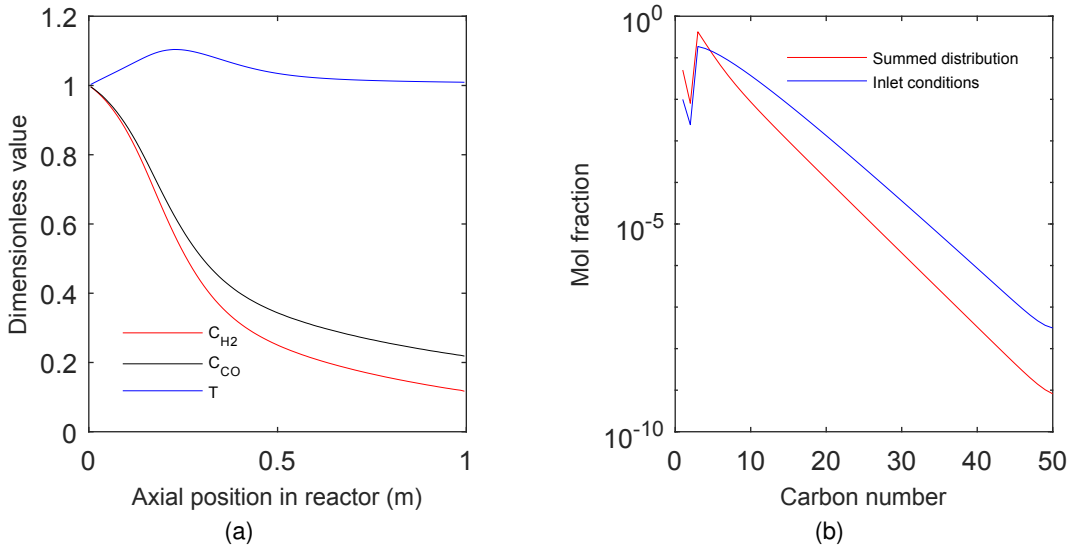

Figure 3.1: (a): Dimensionless profiles over the axial position in the reactor. (b): The found product distribution compared with the product distribution for inlet conditions. Inlet temperature set to 490 K, inlet concentration of H_2 to 50, syngas ratio to 2, particle diameter to 3 mm and the inlet velocity to 0.1 m/s.

The product distribution is found in a similar way as discussed in section 2.1.1. When equation (2.14) is expanded to include the grid cells in the axial direction of the reactor equation (3.5) is found. In this equation the mol fraction per grid cell is found as discussed in section 2.1.1. The equation for the selectivity of C_{5+} products remains as given in equation (2.15). The space time yield is found via equation (3.6).

$$x_n = \frac{\sum_{i=1}^{nTGC}\sum_{j=1}^{nPGC} x_{n,ij} R_{CO,ij} V_{GC,j}}{\sum_{i=1}^{nTGC}\sum_{j=1}^{nPGC} R_{CO,ij} V_{GC,j}} \tag{3.5}$$

$$STY_{C_{5+}} = \frac{\iiint_{V_R} S_{C_{5+}} R_{CO} dV}{V_p/\varepsilon_b} \tag{3.6}$$

3.2 Results

Figure 3.1 shows the results for a simulation of the FTS using typical conditions. In figure 3.1a it can be seen that initially the temperature increases up to 543 K, due to the exothermic reaction. It can also be seen that this temperature rise causes the reactants to disappear faster. As the concentrations of the reactants lower, so does the reaction rate. The temperature here drops again towards the wall temperature. Further it can be seen that the H_2

consumption is bigger than two times the CO consumption, as relatively more H_2 is consumed.

The product distribution found for the reactor model is shown in figure 3.1b. The found selectivity towards C_{5+} products is 0.45 $kg_{C_{5+}}/kg_{product}$ and the space time yield for these products is 58.34 $g\ m^{-3}\ s^{-1}$. The product distribution shows an increase in mainly the first three products compared to the product distribution found for the inlet conditions. The mol fractions found for C_1, C_2 and C_3 products are 0.05, 0.008 and 0.42 mol/mol respectively.

The shape of the ASF plot again shows the methane and ethylene deviations, but does not include the decreasing slope for larger hydrocarbons. Although the methane deviation is present, it should be noted that the production of C_3 products is bigger than that of methane. The latter happens despite the high temperatures present in the reactor and the great syngas ratios in the catalyst particles. Both effects would stimulate the production of methane.

An explanation for these observations could again be the absence of olefin readsorption in this model. Inclusion of readsorption could result in the decreasing slope for the long chain hydrocarbons. Addtionally, it could decrease the production of propylene.

The found value for the selectivity of C_{5+} products is lower than that for the inlet conditions. The production of methane is found to be higher. Compared to the particle model the product selectivity is lower. The production of methane is however also lower. Two effects appear to be affecting the product distribution. First the higher temperature will stimulate the production of shorter hydrocarbon chains. This will cause an increased consumption of H_2 compared to the consumption of CO. The syngas ratio will decrease over the length over the reactor. A lower syngas ratio will then stimulate the production of longer hydrocarbon chains.

3.2.1 Influence of parameters

To observe the trends that the reactor model shows for variation of parameters, 135 reactor simulations are performed. The found product selectivities and space time yields can be found in appendix A. The maximum temperature rise found for these simulations are also given. Some simulations, mainly regarding high temperatures, high concentrations and low particle diameters have diverged. For these conditions it can be expected that the system is more stiff, due to increased heat generation and reaction rates.

For each parameter value, the found selectivities and space time yields are averaged and shown in figure 3.2. The space time yields have been normalized using the highest found average space time yield. For the simulations that have diverged it is assumed that the selectivity and space time yield towards C_{5+} products is zero.

Concentration

On average an increasing concentration lowers the product selectivity. This can be addressed to two effects. The first is described in section 2.2.2. Here it is discussed how, for higher concentrations, a decrease of CO concentration in the particle leads to a higher reaction rate and a lower product selectivity. This effect is not beneficial for the product selectivity.

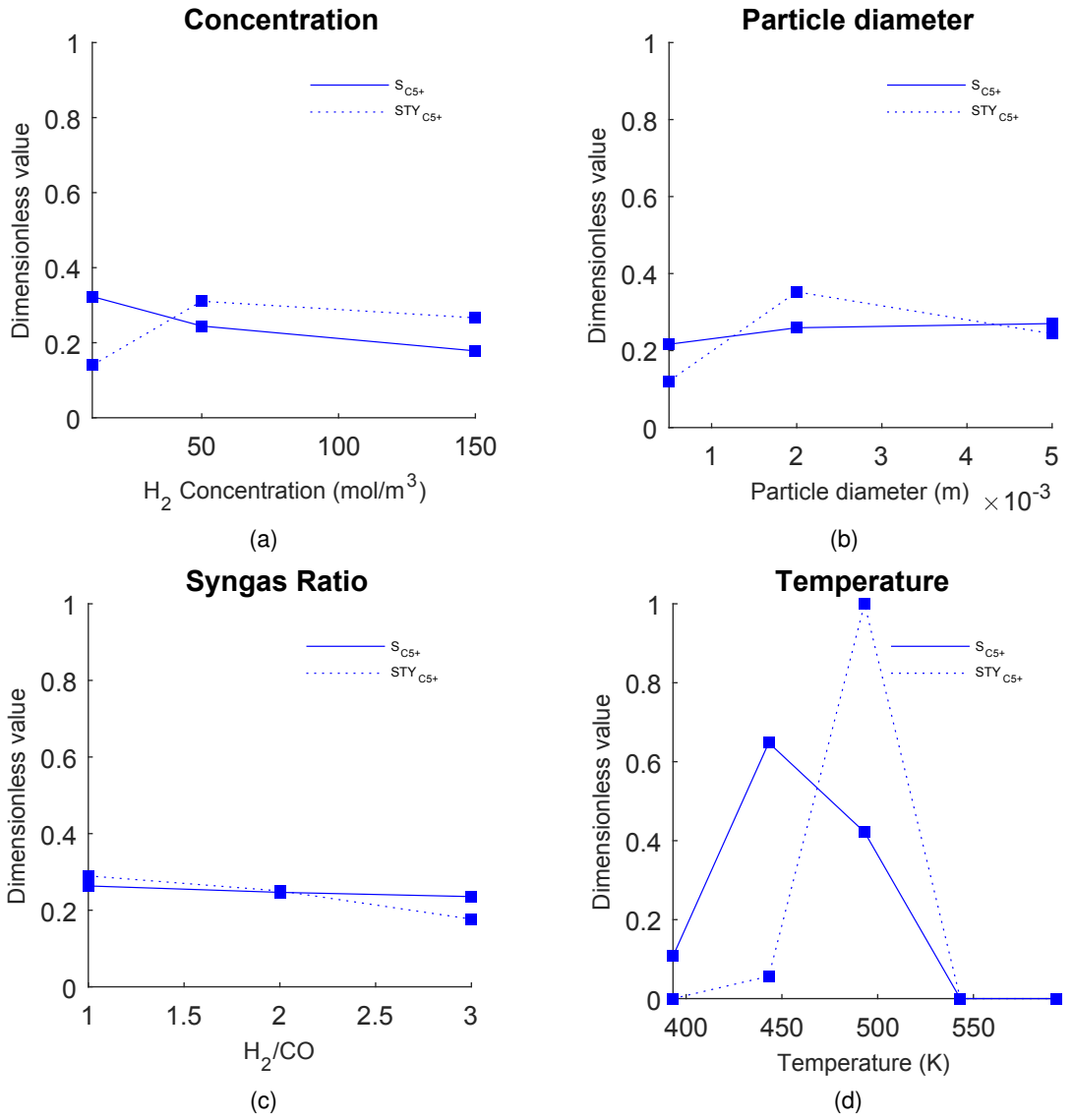

Figure 3.2: Averaged dimensionless values of product selectivity and space time yield for varied (a) Inlet concentration of H_2, (b) Catalyst size, (c) Syngas ratio and (d) Inlet and wall temperature obtained from the one dimensional tubular reactor model.

The second effect of increasing the concentration is that the reaction rate will increase. As the reaction is highly exothermic, this will lead to an increase in temperature, which is shown in table A.2. This will influence the selectivity as discussed in section 2.1.2.

For the space time yield it can be seen that this initially increases with increasing concentration, even tough the selectivity goes down. This is likely because of increased production rates. When the concentration is further increased, the space time yield drops together with the selectivity.

Particle diameter

The biggest effect of decreasing the particle diameter is likely that the temperature increases more due to a higher reaction rate. As can be seen in table A.2 the temperature often becomes much higher for smaller particles. The increase in temperature leads to a lower product selectivity. The space time yield shows an optimum. Although the selectivity decreases for smaller particle sizes, the production rate increases.

Table A.3 also shows cases where smaller particles yield higher selectivities than bigger particles. This could be explained looking at figure 2.3. In this figure it is seen that at some positions in the particle the production rate is higher, while the selectivity is lower, due to the lower concentration of CO. It is possible that in a smaller particle this region does not exist or is smaller.

Syngas Ratio

The effect of varying the syngas ratio appears to be the lowest of the investigated parameters. The product selectivity slightly increases with decreasing ratio and the space time yield follows the same trend. There are however two effects that should be noted before concluding that this parameter does not affect the product distribution.

In table A.3 it can be seen that, for a H_2 concentration of 50 $mol\ m^{-3}$, a particle diameter of $5 \cdot 10^{-3}$ m and a temperature of 493.15 K, the selectivity increases from 0.45 to 0.70 mol/mol when decreasing the syngas ratio. This observed trend matches well with the results shown in figure 2.2.

Other conditions, such as a H_2 concentration of 10 $mol\ m^{-3}$, a particle diameter of $5 \cdot 10^{-3}$ m and a temperature of 443.15 K, cause the selectivity to decrease with decreasing syngas ratio. This once again can be explained looking at the temperature rise in the reactor. This is higher for the lower syngas ratio. This is caused by the way the inlet concentrations are determined.

The inlet concentrations are set by defining the H_2 concentration and then setting the CO concentration according to the syngas ratio. Addition of CO in many cases leads to slower reactions. In this case it however causes bigger temperature increases, as simply more potential energy is fed to the reactor. To better investigate the effect of syngas ratio, simulations where the inlet potential energy is kept constant rather than the inlet H_2 concentration should be performed.

Temperature

Temperature appears to have the biggest effect on the product selectivity and the space time yield. A Sabatier's optimum is found similar to that discussed in section 2.1.2. The optimum is however shifted to a lower temperature. This is likely to be caused by the fact that temperature increases in the reactor due to the exothermic reaction. The highest space time yield is found for temperatures of 493.15 K. While the selectivity is lower for this temperature, the reaction rate appears much higher at this temperature.

Not only based on the temperature sweep it can be concluded that the effect of temperature on this reaction is the greatest according to the model. For the other varied parameters the effect was often dominated by the effect of the parameters on the temperature rise in the reactor. The model confirms that heat management is an important issue for the FTS. Overall the observed trends match well with the expectations and the observations made in section 2.1.2.

To properly test the magnitude of the mentioned effects more research is to be done, as this is only a proof of concept. Many values regarding the energy balance, such as the heat transfer coefficients and the reaction enthalpy are assumed for this system. Further fine tuning of the parameters will not likely change the observed trends, but could influence the magnitude of certain effects compared to the other observed effects.

4 Immersed Boundary Method

4.1 Numerical methods

The used CFD algorithm utilizes the Immersed Boundary Method (IBM). The numerical techniques and discretization shemes as well as the validation for resolving flow and heat transfer in a fixed bed randomly packed with spheres of the used algorithm can be found in the work of Das et al. [47]. For resolving the FTS in the algorithm, mass transfer equations are added to the algorithm. The equations are solved in a similar way as the energy equations using established analogies.

The energy and mass equations become coupled as an exothermal chemical reaction is added. To accomplish this coupling in the model, source terms are added to the energy and mass transfer equations. For the fluid phase the governing equations for energy and mass are thus given by the equations below.

$$\rho_f C_{p,f} \left[\frac{\partial T_f}{\partial t} + \nabla \cdot (\overline{u} T_f) \right] = k_f \nabla^2 T_f \tag{4.1}$$

$$\frac{\partial C_{i,f}}{\partial t} + \nabla \cdot (C_{i,f} \bar{u}) = D \nabla^2 C_{i,f} \tag{4.2}$$

Here $\bar{u}$ the velocity found via the Navier-Stokes equation. For the solid phase the governing equations are given by equations (4.3) and (4.4).

$$\rho_s C_{p,s} \frac{\partial T_s}{\partial t} = k_s \nabla^2 T_s + \sum_{i=1}^{i=nComponents} (-\Delta H_{r,i})\, r_i \tag{4.3}$$

$$\frac{\partial C_{i,s}}{\partial t} = D^{eff} \nabla^2 C_{i,s} + R_i \tag{4.4}$$

In the governing equations i represents the species that is to be solved. The last term in equation (4.3) represents the summation of the reaction enthalpy of all species that are solved.

The program is coded in such a manner that multiple components can be included. The components can be coupled via the reaction term. The updating scheme is given in figure 4.1. First the velocity profile has to be set by solving the Navier Stokes equation. Then the energy equations are solved and the temperature is updated. Before this can be done,

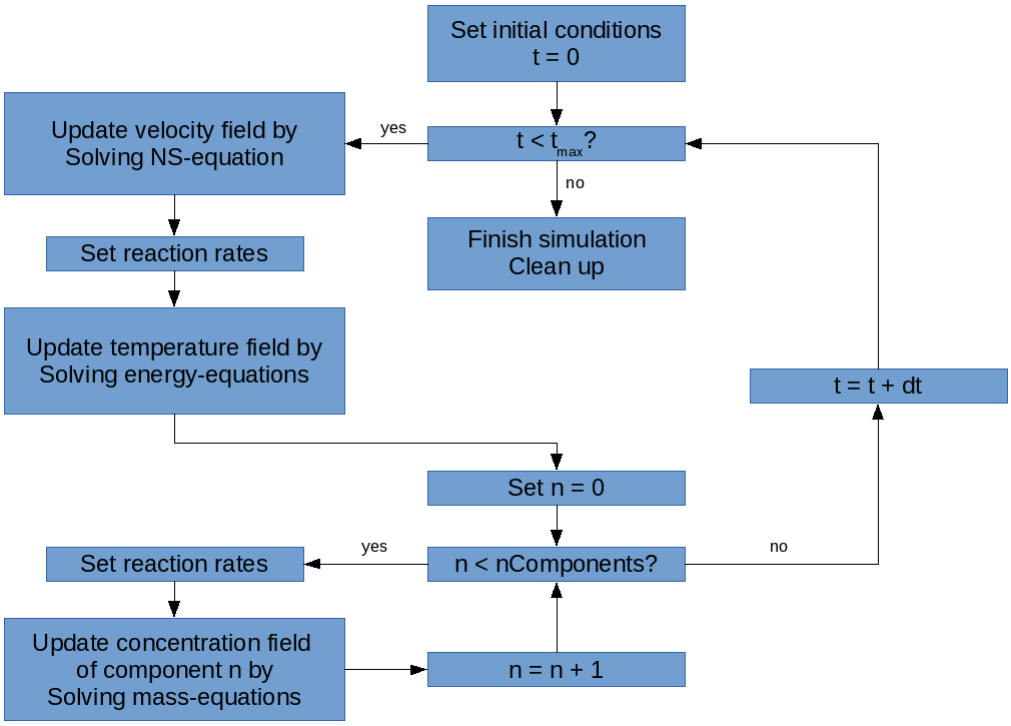

Figure 4.1: flow chart by which the code is solved for a certain amount of time steps

the reaction rate terms are to be set, because it is necessary that the heat generated in the reaction in that time step can be properly taken into account. After updating the temperatures in the grid, the mass transfer equations are solved for each component one by one. Before solving the mass transfer equations for one component, the reaction terms that depend on or influence multiple components are updated.

To check whether different components can be solved independent of each other, simulations are performed using different amounts of components. In the simulations flow and mass transfer are solved. A first order reaction is also added inside the solid particle. The time to solve 200 time steps is clocked. Figure A.1 shows that increasing the amount of components linearily increases the computation time, as is expected.

4.2 Model verification

In order to verify the implementation of the mass transfer equations and their coupling to the energy equations, three verification test cases are simulated. First the simulation of an isothermal diffusion reaction problem in a spherical particle is compared to the analytical solution given by Aris [48]. In the second test case the coupling of the heat and mass equations are tested by comparing simulation results for a non-isothermal first order diffusion reaction problem with the solution given by Weisz and Hicks [49]. In the final test case a global mass balance is computed for flow past a spherical catalyst.

4.2.1 Methods

Isothermal diffusion reaction

As derived by Aris, the effectiveness factor η for a first order reaction in a spherical particle with a constant surface concentrations C_{AR} is given by equation (4.5). Here W_{AR} is the flux of component A through the surface of the particle and $W_{AR,0}$ is the flux of component A through the surface of the particle for the limiting case that diffusion is infinitely fast.

$$\eta = \frac{W_{AR}}{W_{AR,0}} = \frac{3}{\phi^2}\left(\phi \coth \phi - 1\right) \tag{4.5}$$

The Thiele modulus ϕ is given in equation (4.6). With r_p the particle radius, k' the reaction rate constant and D^{eff} the effective diffusivity coefficient in the particle pores.

$$\phi = r_p \sqrt{k' \Big/ D^{eff}} \tag{4.6}$$

Simulations are performed in which the surface concentration of the particle is set constant to 2 mol/m^3 (Dirichlet boundary conditions). The radius of the particle is set to be 1 cm and D^{eff} is set to $10^{-4}\ m^2/s$. A Cartesian 40x40x40 grid is used. The size of one grid cell is $10^{-9}\ m^3$. This means that over the diameter of a particle 20 grid cells are used.

The reaction rate constant is varied such that the Thiele modulus is varied between $\sqrt{1/8}$ and 16. The solid flux is found via the surface integral of the fluxes through the surface computed via the IBM. $W_{AR,0}$ is found by assuming that the surface conditions apply for the whole catalyst particle. This leads to equation (4.7), in which R_0 is the reaction rate corresponding to the conditions at the surface of the particle.

$$W_{AR,0} = {}^{4}\!/_{3}\pi r_p^3 a_p \left(-R_0\right) \tag{4.7}$$

Non-isothermal diffusion reaction

In 1962, Weisz and Hicks developed a correlation between the effectiveness factor and the Thiele modulus for non-isothermal first order reactions in spherical particles with constant surface concentration and temperature [49]. They derived an expression that correlates the effectiveness factor to the reaction specifics and the concentration gradient at the surface of the particle (4.8).

$$\eta = \frac{3}{a\phi_0^2}\frac{dy}{d\xi} \tag{4.8}$$

With a the pre-exponential factor from the Arrhenius type kinetics, y the dimensionless concentration, and ξ the dimensionless reaction radius given in equation (4.9).

$$\xi = \frac{r}{ar_p} \tag{4.9}$$

$$\phi_0 = r_p \sqrt{k_0 / D^{eff}} \tag{4.10}$$

k_0 is in this case the reaction rate constant corresponding to the surface temperature T_0. In order to find the concentration gradient at the surface, a second order ordinary differential equation (ODE) (4.11) has to be solved. Weisz and Hicks solved this equation using a Taylor series expansion. Using modern day computers, the equation can more easily be solved reducing the order. When Y_1 is considered the first variable being equal to y and Y_2 is the second variable being equal to the first derivative of y towards ξ, the system of ODE's becomes as given by equations (4.12) and (4.13).

$$\frac{d^2y}{d\xi^2} + \frac{2}{\xi}\frac{dy}{d\xi} = a^2\phi_0^2 y \exp\left[\gamma\beta\left(\frac{1-y}{1+\beta(1-y)}\right)\right] \tag{4.11}$$

$$\frac{dY_1}{d\xi} = Y_2 \tag{4.12}$$

$$\frac{dY_2}{d\xi} = -\frac{2}{\xi}Y_2 + a^2\phi_0^2 Y_1 \exp\left[\gamma\beta\left(\frac{1-Y_1}{1+\beta(1-Y_1)}\right)\right] \tag{4.13}$$

Here γ is the Arrhenius number and β the maximum temperature variation which could exist in the particle relative to the boundary temperature. The equations for these quantities are given by equations (4.14) and (4.15).

$$\gamma = \frac{E_a}{RT_0} \tag{4.14}$$

$$\beta = \frac{C_0(-\Delta H_R)D^{eff}}{kT_0} = \left(\frac{\Delta T}{T_0}\right)_{\max} \tag{4.15}$$

The system of ODE's is solved using Matlab's ode15s ODE-solver. Simulations are performed where γ is set to 20 and β and ϕ are varied. β is varied from 0.4 to 0.8 and ϕ from 0.3 to 2.0. β is varied by varying the surface temperature and γ is in this case kept constant by adjusting the activation energy. The Thiele modulus is varied by varying the pre exponential factor.

Flow past a sphere

The next step in developing the reactor model is inclusion of flow as is described in section 4.1. For verification of this implementation, the mass balances for the three components are solved. For H_2 and CO at steady state it should hold that the number of moles flowing

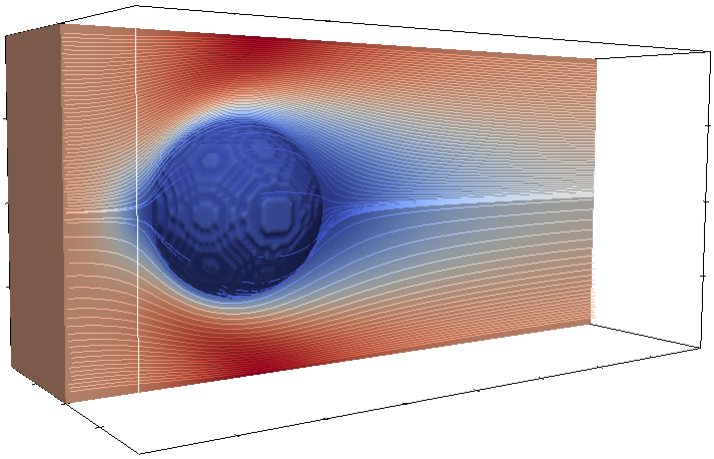

Figure 4.2: Graphical representation of the used system for solving the global mass balance.

in, equal the number of moles flowing out plus the moles that are consumed. The moles flowing in and out can be found performing a surface integral over the in and outlet. The production is found via a volume integral over the particle. This leads to equation (4.16). The production of H_2O is also solved. To see whether this is done correctly, the production of H_2O is compared to the consumption of CO. These should in this case be equal.

$$\iint_A u_0 C_i^{z=0} dA = \iint_A \left[u C_i^{z=L} + D_i \frac{\partial C_i^{z=L}}{\partial z} \right] dA - \iiint_V R_i dV \tag{4.16}$$

To test the mass balance and its dependence on the reaction enthalpy, arbitrary values for the physical properties are used to speed up computation. The parameters used are given in table 4.1. The kinetics used are described by equations (2.8) and (2.3). The reaction rate is multiplied with 25 to establish a notable effect of the reaction. The walls are in this case adiabatic. A visual representation of the system is shown in figure 4.2.

The coupling between the fluid and solid phase is done using conjugated mass and heat transfer boundary conditions. This means that the flux from the solid to the solid surface is equal to the flux from the fluid phase to the solid surface. The conjugated mass transfer boundary condition at the solid interface is given by equation (4.17). The boundary condition for the energy equation is analoge to this equation. The temperature and concentration at the solid surface are found using the IBM. The details of this method are described by Das et al. [12].

$$-D_i \frac{\partial C_i}{\partial \bar{n}} = -D_i^{eff} \frac{\partial C_i}{\partial \bar{n}} \tag{4.17}$$

Table 4.1: Used parameters for performing a global mass balance for flow past a sphere.

Symbol	Description	Value
ρ_f	Fluid density	1000 $kg\ m^{-3}$
μ_f	Fluid viscosity	0.1 Pa s
T_{in}	Inlet temperature	490 K
k_f	Heat transfer coefficient fluid	0.14 $W\ m^{-1}s^{-1}$
Cp_f	Specific heat fluid	1 $kJ\ mol^{-1}\ K^{-1}$
u_0	Inlet velocity	0.1 $m\ s^{-1}$
k_s	Heat transfer coefficient solid	0.5 $Wm^{-1}s^{-1}$
Cp_s	Specific heat solid	10 $J\ mol^{-1}\ K^{-1}$
ρ_s	Solid density	1000 $kg\ m^{-3}$
D	Diffusion coefficient	$1 \cdot 10^{-4}\ m^2\ s^{-1}$
$C_{H_2,in}$	Inlet concentration H_2	50 $mol\ m^{-3}$
$C_{CO,in}$	Inlet concentration CO	25 $mol\ m^{-3}$
ϵ_{TP}/τ_{TP}	Obstruction in catalyst pores	1.0
	Cartesian grid	80x40x40
	Grid cell size	$10^{-3^3}\ m^3$
r_p	Particle radius	1 cm
dt	time step size	$1 \cdot 10^{-4}$ s
ΔH_R	Reaction enthalpy	0 - 160 $kJ\ mol^{-1}$

4.2.2 Results

Thiele test case

The results generated for the test case can be found in table A.5. The found effectiveness factors are displayed in figure 4.3a together with the analytical solution.

As can be seen in figure 4.3a the found effectiveness factors match the analytical solution well. For low Thiele moduli the error is approximately 0.22 %. When the Thiele modulus exceeds the value 4, the found effectiveness factor becomes smaller than the calculated effectiveness factor. From this value onwards, it can be seen that the error increases rapidly towards -3.24 % for a Thiele modulus of 16. It is however also shown that increasing the amount of grid cells by a factor 2^3 can significantly decrease this error to -1.22 %. When the simulation is run with various components that are not coupled, identical results are acquired, as is expected.

Weisz and Hicks test case

Figure 4.3b shows the results of the non-isothermal diffusion reaction simulations. The results are more precisely given in tabel A.6 in appendix A. The results that are found, are similar in trends as those observed for the isothermal diffusion reaction problem. The results match the expected values well, both for the lower steady state temperature and the higher steady state temperature.

The deviations from the analytical solution become bigger as the Thiele modulus increases.

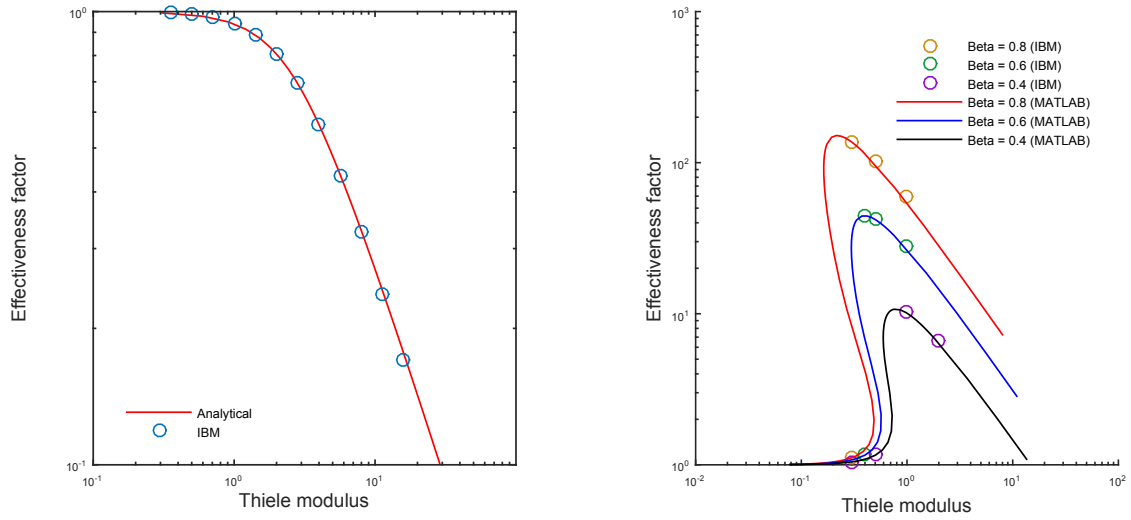

(a) (b)

Figure 4.3: a: Effectiveness factors computed for isothermal diffusion reaction in a sphere compared to the effectiveness factor as calculated via the analytical solution. b: Effectiveness factors computed for non-isothermal diffusion reaction in a sphere compared to the effectiveness factor as calculated via the analytical solution as proposed by Weisz and Hicks for γ equal to 20.

The deviation also appears to grow with increasing the maximum adiabatic temperature rise of the particle. Furthermore, the deviations are smaller for the smaller steady state values than the higher steady state values. The lowest deviation is found for the lower steady state value for β equal to 0.8 and ϕ equal to 0.3. This error is only 0.11 %. The highest error is found for β equal to 0.8 and ϕ equal to 1.0. This error is larger with 9.47 %.

Flow past a sphere

The results of the global mass balance are given in table A.7, A.8 and A.9. The global mass balance holds well for systems with lower reaction enthalpies. The deviation from the mass balance greatly increases when the reaction enthalpy is increased. The deviation is smaller for CO than for H_2.

For H_2 the deviation is only 0.27 % for the isothermal case. This increases up to even 67.74 % for a reaction enthalpy of -160 kJ/mol. In the previous verification cases it was already concluded that increased reaction rates and increased reaction enthalpies increase the deviation. Although the effectiveness factor does not directly influence the mass balance, the same trend is observed.

For CO the deviations are smaller than for H_2. This is possibly because the reaction rate of H_2 is higher than that of CO. The Deviation of H_2O might indicate the cause for the mass imbalance. Here it clearly can be seen that the moles produced do not reach the outlet of the system. The production rate of H_2O does perfectly match with the consumption rate of CO.

Table 4.2: Mass balance of the flow past a sphere test for a coarse grid (20 grid cells/d_p) and a more refined grid (40 grid cells/d_p). Reaction enthalpy was set to -20 kJ/mol. The balance error represent the deviation of the global mass balance. The flux error represents the difference between the flux from the fluid phase to the solid phase compared to the total reaction rate in the solid particle.

Grid cells/dp	Species	In (mol/dt)	Out (mol/dt)	Production (mol/dt)	Balance error (%)	Solid Flux (mol/dt	Flux error (%)
20	H2	8.54E-07	7.29E-07	-1.89E-07	-7.48	-1.75E-07	7.40
	CO	4.27E-07	3.68E-07	-8.74E-08	-6.69	-8.12E-08	7.13
	H2O	0.00	5.89E-08	8.74E-08	-48.49	8.12E-08	7.13
40	H2	8.54E-07	7.32E-07	-1.32E-07	-1.17	-1.31E-07	0.76
	CO	4.27E-07	3.69E-07	-6.29E-08	-1.15	-6.25E-08	0.64
	H2O	0.00	5.81E-08	6.29E-08	-8.26	6.25E-08	0.64

In theory the total reaction rate in the solid should be equal to the flux towards the solid in steady state. For the isothermal case they are equal. Increasing the reaction enthalpy also enlarges this difference.

Increasing the reaction enthalpy increases the temperature and thus the reaction rate. A higher reaction rate causes a lower concentration in the solid. This then causes a greater concentration gradient over the solid surface. The bigger gradient could cause a decrease in the accuracy and thus the mass balance. If this is indeed the problem, then the accuracy likely depends on the grid refinement.

An extra simulation is performed in which the sensitivity towards grid refinement is investigated. In this run the reaction enthalpy is set to -20 kJ/mol. The results of this test are given in table 4.2. The results clearly show that the grid refinement grealty influences the accuracy of the simulation. For the simulation in which 8 times more grid cells are used, the deviations are approximately 6 times smaller. The mass balance is considered to be satisfied. The grid refinement dependency should however be taken into account when performing simulations, as it apears that the accuracy of a simulation is sensitive to the reaction properties.

4.3 Implementation of Fischer Tropsch Synthesis

4.3.1 Diffusion reaction problem

Methods

The kinetics described by Yates and Satterfield (section 2.2.1) are implemented in the IBM code. As the FTS has not before been implemented in a three dimensional DNS it is important to see how the model performs compared to the created one dimensional model. As the implementation of the α-correlation is less extensive and time consuming, this part is first done using this correlation rather than using the micro kinetic model.

Implementing the model is done as it is done as described in section 2.2.1. The determination of the product selectivity is however done differently. As the IBM uses a Cartesian grid, all grid cells have the same size and no correction is needed anymore for taking into account different grid cell volumes. This is already included as there are simply more grid cells near the surface of the particle than in the center. Additionally solving the problem in

three dimensions greatly increases the amount of data that should be stored and processed. For these reasons the product selectivity is computed in an alternative way.

After a certain amount of time steps, the probability is determined in every grid cell of the simulation grid. This is possible, as the concentrations of H_2 and CO and the temperature are known in every grid cell and the rest of the parameters are constants. Since the concentration ratios and temperature can be different in different cells, different probabilities are found within both the reactor as a single particle.

When the value of α in a grid cell is determined, the reaction rate in the corresponding grid cell is stored into a bin. A certain amount of bins (nBins) is set. The size of the bin (binSize) is then equal to 1/nBins. The bin corresponding to a given α can be determined by taking the lower integer from $\alpha/binSize$. Once the corresponding bin is found, the value of the reaction rate in that grid cell is added to both that bin as a dummy variable that tracks the total reaction rate that is stored. The total reaction rate is later used to normalize the found distribution by dividing the values in all the bins by it.

The found distribution of propagation probabilities is converted to a product distribution by using the ASF-model (2.2). When this equation is expanded towards a weighted summation of product distributions, the mole fraction of a component is given by equation (4.18):

$$x_n = \sum_{i=0}^{i=nBins} (1-\alpha(i))\alpha(i)^{n-1} \cdot weight_{\alpha(i)} \tag{4.18}$$

In which n is the carbon number and $\alpha(i)$ is the propagation probability bin i. The latter is determined by taking the average value of the probabilities that could have been stored in the bin. Weight stands in this equation for the normalized reaction rate stored in the bin. After the mol fractions are determined, the selectivity is again determined using equation (2.15). The effectiveness factor is again determined using equation (4.5). For solving the diffusion reaction problem the parameters in table 2.1 are used.

Results

As can be seen in figure 4.4 the diffusion reaction problem yields similar results when it is solved using the IBM. When the results are compared to those of the one dimensional model, shown in figure 4.4a, the same profiles are found. This is confirmed when the effectiveness factor and the product selectivity are determined. An effectiveness factor of 0.93 was found and a product selectivity of 0.83 $kg_{C_{5+}}/kg_{product}$ using the IBM. These values both deviate less than 1 % from the values obtained via the one dimensional model.

A simulation is also performed in which equation (4.3) is also solved. The simulation run stable with the used grid and time step size. The maximum temperature rise found was 0.60 Kelvin, which matches the values found in the 1-D particle model.

The time needed to reach steady state for the isothermal case was approximately 120 seconds. For the non-isothermal case this was 450 seconds. Both these times can be considered long for DNS. The long time for the isothermal case is caused by the slow intraparticle diffusion. The time needed to reach steady state increases when the coupling with the energy balance is made. As the temperature depends on the reaction rate and the reaction

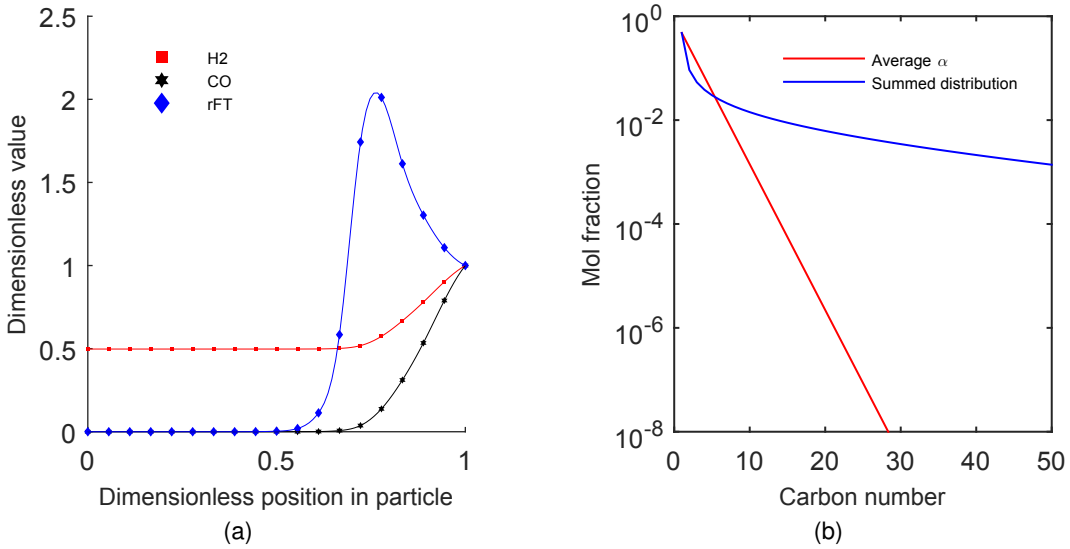

Figure 4.4: Results isothermal reaction diffusion model Yates and Satterfield kinetics, T = 490 K, $d_p = 3\ mm$, P = 20 bar, $C_{\mathrm{H}_2,s} = 50\ mol\ m^{-3}$, $C_{\mathrm{CO},s} = 25\ mol\ m^{-3}$, a: Dimensionless results of the particle model, with position 0 the centre and 1 the surface of the particle b: product distribution for average α and for the weighted sum of local distributions.

rate depends on the temperature, an iterative problem is present. This causes the simulation to take more time to reach steady state.

4.3.2 Cylindrical packed bed reactor

Methods

Das et al. [47] generated fixed bed reactors randomly packed with spheres. The packing described in this paper with N = 4, i.e. 4 spheres over the reactor diameter, is used to test the FTS implementation. Of this packing only the first 30 spheres are used to make the system smaller. The parameters are set as given in tables 2.1 and 3.2. In addition, in order to solve the Navier Stokes equation, the viscosity is set to $1.6 \cdot 10^{-6}\ Pa \cdot s$.

As stated in section 4.3.1 the slow diffusion of the syngas causes the need for long simulations. To generate a proof of concepts for the FTS in the DNS and to investigate the simulation time that would be needed, the diffusion coefficient is increased by a factor 1000. For solving the bed to wall heat transfer, instead of using Newton's law for cooling, boundary conditions are applied at the wall. The wall temperature is set to be constant and equal to the inlet temperature of 490 Kelvin.

For creating of the cylinder a Cartesian grid of 300x82x82 grid cells with a size of $(1.5 \cdot 10^{-4})^3$ m^3 is used. The spheres are placed approximately $1.3 \cdot 10^{-2}$ m from the tube entrance. Behind the packing approximately $2.5 \cdot 10^{-2}$ m of empty tube is placed. The empty tube space in front of and behind the particles is necessary for stabilizing the flow and thus system. The time step size that is used is $1 \cdot 10^{-4}$ s

Results

Figure 4.5 shows a visual of the packed bed reactor. The visual is not made at steady state. Due to the slow diffusion of the syngas and the costly computation of the DNS, it is estimated that reaching of steady state for this system will take multiple years. Still it is possible to conclude that the FTS is properly implemented and that a three dimensional model can lead to insights regarding the FTS.

The consumption of CO and H_2 showed similar figures. As can be seen in figure 4.5a, the syngas is being consumed in the particles quickly. As the syngas dissapears, figure 4.5b shows that water is created as is expected.

In figure 4.5c the development of temperature is shown. The temperature profile over the cylinder is shown in figure 4.6. It can be seen that from the catalyst particles heat is generated. It can also be seen that the temperature decreases when getting closer to the wall. The particles in the middle are heated up the most. The highest temperature found in the packing is 620 K.

The averaged temperature profile shows a similar profile as is found for the 1D reactor model. The system heats up as the reaction starts and approaches the wall temperature when the reactants are mostly reacted. The highest temperature in the profile is 548 K. This is 72 K lower than the found hot spot of 620 K. Both the FTS selectivity models investigated in chapter 2 indicate that at these temperatures only methane will be produced. The production rate at this temperature will also be higher, increasing the effect of these hot spots. Although this is only a proof of concept, the need for three-dimensional reactor models of the FTS is illustrated by these results.

Simulation time

For investigation of the time needed to have such a simulation reach steady state, the time needed to solve one time step is investigated. Every time step consists of three parts. The first part is the Navier Stokes solver to set the velocity profile, the second part is the energy solver to set the temperature profile and the third part is the mass equations solver to set the concentration profiles. Averaged over 100 time steps the computational time needed for solving the parts is approximately 53, 54 and 67 seconds per time step respectively. Assuming that simulating 110 seconds of real time is necessary for reaching 1 % from steady state and that solving the Navier Stokes equation is no longer needed after 4 real time seconds, the estimated simulation time for this system is about 4 years. Usage of parallel computation could in the current code reduce the computational time to approximately 0.75 years.

The estimated simulation time is based on the assumption that reaching steady states for this system takes an equal amount of real time as the non-isothermal diffusion reaction problem. The addition of convection likely increases this time more. Further, the used grid is such that 20 grid cells are present over the particle diameter. Based on the results found in section 4.2 it can be argued that a more refined grid is needed. As the Thiele modulus of the reaction is high and the reaction is highly exothermic, bigger inaccuracy is likely. Additionally, the current system applies 30 spheres. A more accurate simulation of the industrial case possibly should include more particles.

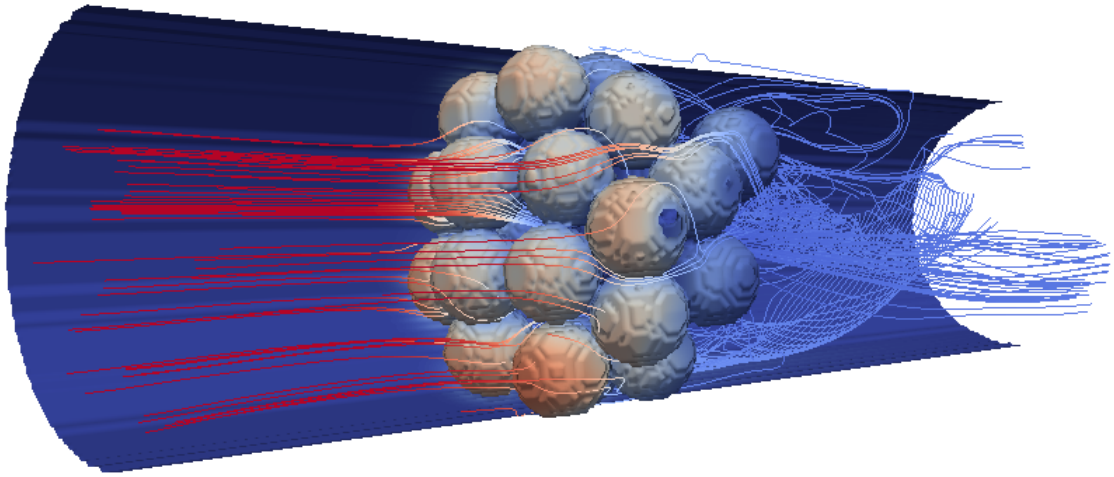

(a)

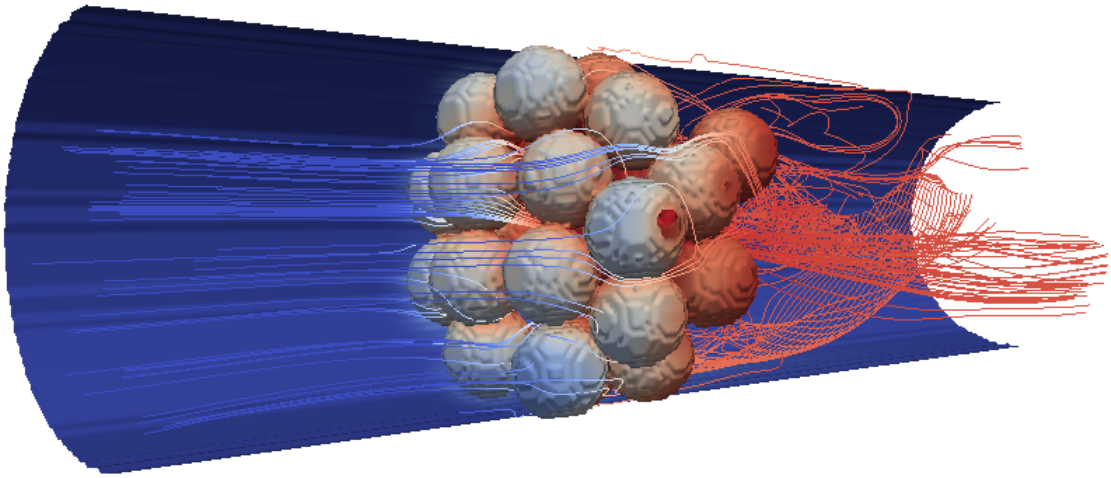

(b)

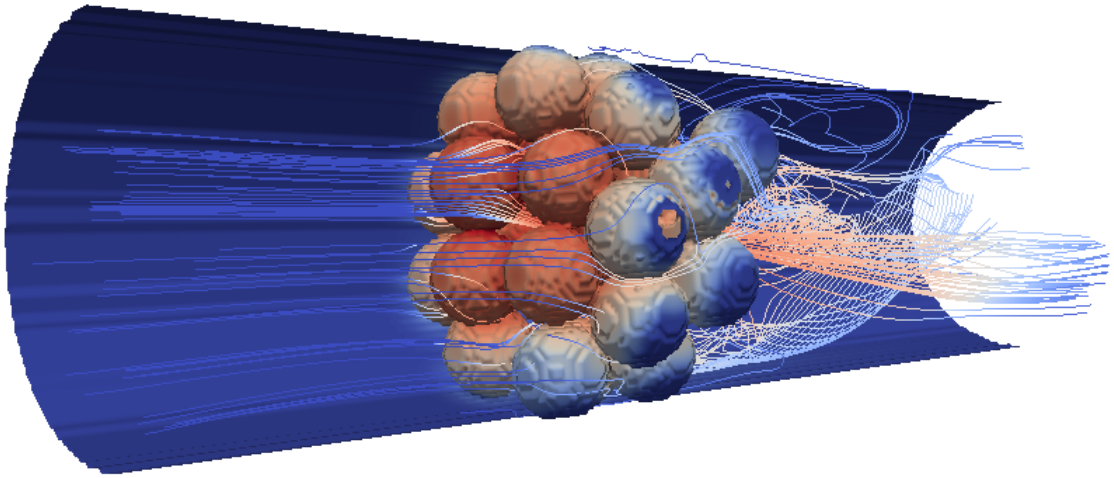

(c)

Figure 4.5: Fischer Tropsch Synthesis implemented in a cylindrical bed packed with 30 spheres. a: The flow of CO, b: The flow of H_2O and c: The distribution of temperature

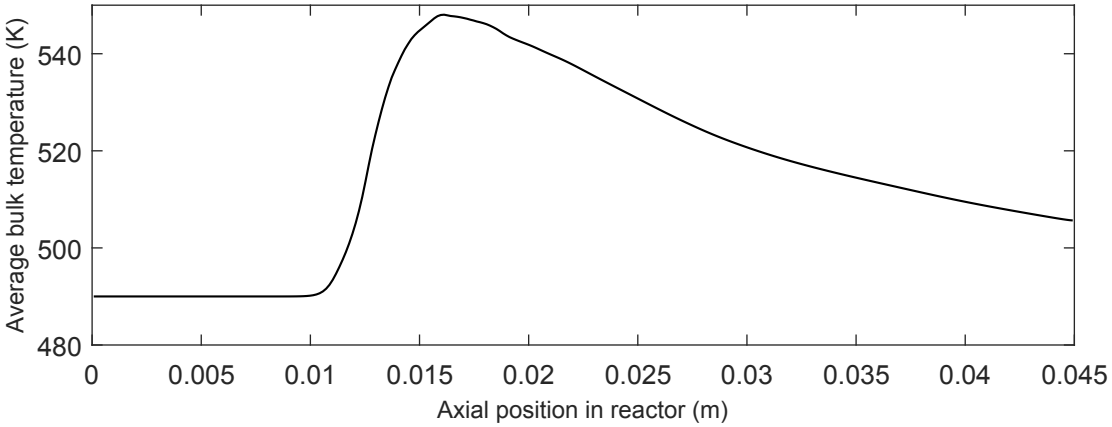

Figure 4.6: Average temperature profile of the FTS in a cylinder packed with 30 spherical catalyst particles.

The three mentioned facts above will likely increase the simulation time further. In order to estimate the computation time for a bigger system a test is done for a system of 163 particles and a grid where the amount of grid cells over the particle diameter is 40. Using the same methodology as described above, the simulation time needed to reach 1 % from steady state would be more than 10 years.

Two main causes can be assigned for the long simulation time. The first is the slow diffusion inside the catalyst pores compared to the convection in the fluid. Due to the slow diffusion long real time is needed for the simulation to finish. Because of the simultaneous solving of the convection, the used time step is forced to be small. The second cause is the highly exothermic reaction. The dependency of the heat generation and the reaction rate cause need for more iterations and thus longer simulation time. Iterating would however likely be faster if the diffusion would be faster.

An attempt is made to reduce the computational time by increasing the time step size after 4 simulated real time seconds. After this time, the velocity profile is steady and stopped being resolved. Increasing of the time step at this point however caused instability in the simulation. The instability possibly finds its root at the convection term.

In order to make the simulation feasible, ways to decrease the simulation time should be investigated. Adaption of certain algorithms in the code can increase the computation time. The biggest problem is however that the convection and intra particle diffusion happen on different time scales when being solved.

It could be investigated whether the convection terms can be solved implicitly rather than explicity. This will increase the stability when bigger time steps are used. Additionally parts of the algorithm can be changed to enhance simulation time. Each time step the type of a grid cell is determined, while the coordinates of cell types are known. Looping over the coordinates of the types rather than the whole system will decrease the computation time.

5 Conclusion and recommendations

Conclusions

The aim of this work was to investigate the implementation of the Fischer Tropsch Synthesis (FTS) in a Direct Numerical Simulation (DNS) that uses the Immersed Boundary Method (IBM). First two selectivity models, a derived correlation by Vervloet et al. and a micro kinetic model by Filot et al., were compared. These models were both implemented in a particle model to solve the diffusion reaction problem. The micro kinetic model was used in a one dimensional reactor model and the correlation was used to investigate the feasibility of the implementation of the FTS in the DNS.

Differences were observed between the two tested selectivity models. For determining the reaction rate of H_2 and the selectivity towards C_{5+} products the correlation showed a straightforward and stiff dependence on the syngas ratio and temperature. These dependencies showed to be more extensive using the micro kinetic model.

With the use of spline interpolation it was possible to implement the micro kinetic model in a particle model. The implementation of the selectivity models in the particle model yielded slightly different results regarding the concentration profiles in the particle. The differences regarding the effectiveness factor and product selectivity were bigger. Here a higher effectiveness factor and a much lower product selectivity were found for the micro kinetic model compared to the correlation. For both models the product selectivity for the particle model was lower than for the bulk conditions. The lower selectivity was caused by the different intraparticle diffusion speeds of the syngas. This effect showed to be smaller for lower syngas concentrations.

The product distribution also showed to be different for both models. The correlation showed a decreasing slope in the ASF-plot, but did not include the methane and ethylene deviation. The micro kinetic model showed the methane and ethylene deviation, but not the decreasing slope. The first model would indicate that the decreasing slope is a consequence of diffusion limitations. The micro kinetic model however indicated that this is not likely. The micro kinetic model is more extensive and likely better able to handle the extreme syngas ratios found in the particle, as it is based on statistical thermodynamics. This model is validated for many aspacts, but not for the specific reaction diffusion problem. As such a micro kinetic model was first implemented in a particle model in this work, this was also not yet possible.

The micro kinetic model was used in a one dimensional reactor model. The effect of particle diameter, inlet H_2 concentration, feed syngas ratio and inlet/wall temperature were investigated. The reactor model showed results in the expected trends. The influence of the particle diameter and syngas ratio showed contradicting effects. Smaller particles and lower syngas

ratios stimulate the product selectivity. They in this case also caused a greater temperature rise in the reactor, which stimulates the production of smaller hydrocarbons. Increasing the inlet H_2 concentration caused a decrease in product selectivity due to increased temperature rise and intraparticle diffusion limitations. When the temperature was varied, Sabatier's optimum was be found. This is however shifted due to temperature rises in the reactor.

The IBM code reported by Das et al. is expanded to handle chemical reactions. The model is verified by solving the diffusion reaction problem and the global mass balance. The model has shown to become less accurate for high Thiele moduli and increased heat generation due to chemical reactions. For high Thiele moduli and reaction enthalpies greater gradients are present at the solid surface. This likely influences the accuracy of the model. The accuracy showed to depend on the grid refinement.

Finaly the FTS is implemented in a cylindrical reactor model packed with 30 spherical catalyst particles. The simulation runs stable and has shown it's value as three dimensional effects as hot spots are observed. A hot spot of 620 K was found, while the average temperature was only 540 K. Improvements to reduce the computational time have however shown to be necessary. The estimated time to finish the FTS simulations is multiple years.

Recommendations

In this work a big step towards a FTS reactor model, in which less assumptions are made, is set. The made model however has drawbacks and still assumptions are present that could influence the outcome of the model. The biggest drawback of the three dimensional model is that it appears to be too computationally costly. A simulation of a small part of the reactor is estimated to take several years using the current methods. Ways to reduce this computation time are to be investigated in order to make the model feasible. The long computational time is caused by the fact that the slow intraparticle diffusion is to be solved using a time step small enough to solve the convection terms.

Solving the convection term implicitly rather than explicitly could increase the stability of the simulation and could allow greater time step sizes to be used. Additionally some smaller changes can be made to speed up the simulation to some extend. In the code currently a big loop over the grid is done. In this loop it is constantly checked what the type of a grid cell is, while it is know what grid cell types are located at specific coordinates. Creating three separate loops for the solid phase, fluid phase and the wall boundaries will decrease the time necessary to loop over the grid.

In the 1D particle model two selectivity models were investigated. The micro kinetic model shows that the methane and ethylene deviations to the ASF plot are present, but the decreasing slope is not. The correlation shows the decreasing slope, but not the methane and ethylene deviations. Micro kinetic models as used in this work are not before applied in particle models or reactor models. The validation of this model is therefor not yet done. Experiments are to be performed to test the validity of this model.

The micro kinetic model does not show a decreasing slope for either the particle or the reactor model. For the reactor model an increased production of C_{3-} products was found. The production of propylene is potentially lower when olefin readsorption would be included in the model. This inclusion possibly also leads to the decreasing slope often observed in

FTS experiments. It is worth investigating whether readsorption of olefins, according to this model, indeed leads to the observed decreasing slope.

In the particle models the diffusion of H_2 and CO have a big influence on the outcome of the simulation results. The diffusion is however modelled based on two assumptions. The first assumption is that the diffusion coefficient is constant. The second assumption is that the syngas diffusion is not influenced by interactions with the liquid wax inside the catalyst pores. For the elimination of the first assumption, a different discretization scheme is to be applied. For the elimination of the second assumption, Maxwell-Stefan diffusion can be applied instead of Fick's diffusion.

Bibliography

[1] Chunshan Song. “Global challenges and strategies for control, conversion and utilization of CO2 for sustainable development involving energy, catalysis, adsorption and chemical processing”. In: *Catalysis Today* 115.1-4 (2006), pp. 2–32. ISSN: 09205861. DOI: 10.1016/j.cattod.2006.02.029.

[2] C. Arden Pope and Douglas W. Dockery. “Health effects of fine particulate air pollution: Lines that connect”. In: *Journal of the Air and Waste Management Association* 56.6 (2006), pp. 709–742. ISSN: 21622906. DOI: 10.1080/10473289.2006.10464485.

[3] F. Fischer and H. Tropsch. “No Title”. In: *Brennst.-Chem* 4.4 (1923), pp. 276 –285.

[4] Gerard P. van der Laan. *Kinetics, Selectivity and Scale Up of the Fischer-Tropsch Synthesis*. 1999, pp. 1–251. ISBN: 9036710111. DOI: 10.1081/CR-100101170.

[5] Ilkka Hannula and Esa Kurkela. “Liquid transportation fuels bed gasification of lignocellulosic biomass”. In: (2013), pp. 1–126.

[6] S. S. Bharadwaj and Lanny D. Schmidt. “Catalytic Partial Oxidation of Natural Gas to Syngas”. In: *Fuel Processing Technology* 42.2-3 (1995), pp. 109–127. ISSN: 03783820. DOI: 10.1016/0378-3820(94)00098-E.

[7] Giovanni Sorda, Martin Banse, and Claudia Kemfert. “An overview of biofuel policies across the world”. In: *Energy Policy* 38.11 (2010), pp. 6977–6988. ISSN: 03014215. DOI: 10.1016/j.enpol.2010.06.066.

[8] Olga Glebova. *Gas to Liquids: Historical Development and Future Prospects*. NG 80. 2013, p. 47. ISBN: 9781907555848.

[9] M.A. Bassiony, Amr Ibrahim, and M.M. El-Kassaby. “An experimental study on the effect of using gas-to-liquid (GTL) fuel on diesel engine performance and emissions”. In: *Alexandria Engineering Journal* 55.3 (2016), pp. 2115–2124. ISSN: 11100168. DOI: 10.1016/j.aej.2016.06.026.

[10] Ralph A Cherrillo et al. “Assessment of Environmental Impacts of Shell GTL Fuel”. In: *Methodology*. 2006.

[11] A.P. Steynberg et al. “Fischer-Tropsch Reactors”. In: *Studies in Surface Science and Catalysis* 152 (2004), pp. 64–195. ISSN: 0167-2991. DOI: 10.1016/S0167-2991(04)80459-2.

[12] Saurish Das, Niels G. Deen, and J. A. M. Kuipers. “Direct numerical simulation for flow and heat transfer through random open-cell solid foams: Development of an IBM based CFD model”. In: *Catalysis Today* 273 (2016), pp. 140–150. ISSN: 09205861. DOI: 10.1016/j.cattod.2016.03.048.

[13] Carlo Giorgio Visconti, Gianpiero Groppi, and Enrico Tronconi. “Highly conductive packed foams: A new concept for the intensification of strongly endo- and exo-thermic catalytic processes in compact tubular reactors”. In: *Catalysis Today* 273 (2016), pp. 178–186. ISSN: 09205861. DOI: 10.1016/j.cattod.2016.02.060.

[14] R. B. Anderson et al. *Physical chemistry of the fischer-tropsch synthesis*. 1959.

[15] Olusola O. James et al. “Reflections on the chemistry of the Fischer-Tropsch synthesis”. In: *RSC Advances* 2.19 (2012), p. 7347. ISSN: 2046-2069. DOI: 10.1039/c2ra20519j.

[16] Branislav Todić et al. “Opportunities for intensification of FischerâĂŞTropsch synthesis through reduced formation of methane over cobalt catalysts in microreactors”. In: *Catal. Sci. Technol.* 5.3 (2015), pp. 1400–1411. ISSN: 2044-4753. DOI: 10.1039/C4CY01547A.

[17] Ivo A W Filot, Rutger A. Van Santen, and Emiel J M Hensen. “The optimally performing Fischer-Tropsch catalyst”. In: *Angewandte Chemie - International Edition* 53.47 (2014), pp. 12746–12750. ISSN: 15213773. DOI: 10.1002/anie.201406521.

[18] Enrique Iglesia. “Design, synthesis, and use of cobalt-based Fischer-Tropsch synthesis catalysts”. In: *Applied Catalysis A: General* 161.1-2 (1997), pp. 59–78. ISSN: 0926860X. DOI: 10.1016/S0926-860X(97)00186-5.

[19] I. Puskas and R. S. Hurlbut. “Comments about the causes of deviations from the Anderson-Schulz-Flory distribution of the Fischer-Tropsch reaction products”. In: *Catalysis Today* 84.1-2 (2003), pp. 99–109. ISSN: 09205861. DOI: 10.1016/S0920-5861(03)00305-5.

[20] Katrina D. Kruit et al. “Selectivity of the Fischer-Tropsch Process: Deviations from Single alpha Product Distribution Explained by Gradients in Process Conditions”. In: *Catalysis Science & Technology* 3.9 (2013), pp. 2210–2213. ISSN: 2044-4753. DOI: 10.1039/c3cy00080j.

[21] M. R. Kamali et al. “A multi-component two-phase lattice Boltzmann method applied to a 1-D Fischer-Tropsch reactor”. In: *Chemical Engineering Journal* 207-208 (2012), pp. 587–595. ISSN: 13858947. DOI: 10.1016/j.cej.2012.07.019.

[22] G. Lozano-Blanco et al. “Extension de la methodologie des evenements constitutifs de la catalyse metallique: Application de la synthyse Fischer-Tropsch”. In: *Oil and Gas Science and Technology* 66.3 (2011), pp. 423–435. ISSN: 12944475. DOI: 10.2516/ogst/2009075.

[23] R a van Santen et al. “Mechanism and microkinetics of the Fischer-Tropsch reaction.” In: *Physical chemistry chemical physics : PCCP* 15.40 (2013), pp. 17038–63. ISSN: 1463-9084. DOI: 10.1039/c3cp52506f.

[24] Mohammad Ostadi, Erling Rytter, and Magne Hillestad. “Evaluation of kinetic models for Fischer-Tropsch cobalt catalysts in a plug flow reactor”. In: *Chemical Engineering Research and Design* 114.3 (2016), pp. 236–246. ISSN: 02638762. DOI: 10.1016/j.cherd.2016.08.026.

[25] I C Yates and C N Satterfield. “Intrinsic Kinetics of the Fischer-Tropsch Synthesis on a Cobalt Catalyst”. In: *Energy & Fuels* 5.1 (1991), pp. 168–173. ISSN: 0887-0624. DOI: 10.1021/ef00025a029.

[26] C. Maretto and R. Krishna. “Modelling of a Bubble Column Slurry Reactor for Fischer-Tropsch Synthesis”. In: *Catalysis Today* 52.2-3 (1999), pp. 279–289. ISSN: 09205861. DOI: 10.1016/S0920-5861(99)00082-6.

[27] F Gideon Botes, Braam van Dyk, and Craig McGregor. “The Development of a Macro Kinetic Model for a Commercial Co/Pt/Al2O3 Fischer- Tropsch Catalyst”. In: *Industrial & Engineering Chemistry Research* 48.23 (2009), pp. 10439–10447. ISSN: 0888-5885. DOI: 10.1021/ie900119z.

[28] Wu Jianmin et al. “Diffusion and Reaction Model of Catalyst Pellets for Fischer-Tropsch Synthesis”. In: *China Petroleum Processing & Petrochemical Technology* 15.4 (2013), pp. 77–86. ISSN: 1008-6234.

[29] Henning Becker, Robert Güttel, and Thomas Turek. “Enhancing internal mass transport in Fischer-Tropsch catalyst layers utilizing transport pores”. In: *Catal. Sci. Technol.* 6.1 (2016), pp. 275–287. ISSN: 2044-4753. DOI: 10.1039/C5CY00957J.

[30] Andreas Jess and Christoph Kern. “Modeling of multi-tubular reactors for Fischer-Tropsch synthesis”. In: *Chemical Engineering and Technology* 32.8 (2009), pp. 1164–1175. ISSN: 09307516. DOI: 10.1002/ceat.200900131.

[31] Vadim S. Ermolaev et al. “Laboratory and pilot plant fixed-bed reactors for Fischer-Tropsch synthesis: Mathematical modeling and experimental investigation”. In: *Chemical Engineering Science* 138 (2015), pp. 1–8. ISSN: 00092509. DOI: 10.1016/j.ces.2015.07.036.

[32] F. Gideon Botes. “Proposal of a new product characterization model for the iron-based low-temperature Fischer-Tropsch synthesis”. In: *Energy and Fuels* 21.3 (2007), pp. 1379–1389. ISSN: 08870624. DOI: 10.1021/ef060483d.

[33] Branislav Todic et al. “Kinetic Model of FischerâĂŞTropsch Synthesis in a Slurry Reactor on CoâĂŞRe/Al 2 O 3 Catalyst”. In: *Industrial & Engineering Chemistry Research* 52.2 (2013), pp. 669–679. ISSN: 0888-5885. DOI: 10.1021/ie3028312.

[34] Minhaj M. Ghouri et al. “Multi-scale modeling of fixed-bed Fischer Tropsch reactor”. In: *Computers and Chemical Engineering* 91 (2015), pp. 38–48. ISSN: 00981354. DOI: 10.1016/j.compchemeng.2016.03.035.

[35] Carlo Giorgio Visconti et al. “Detailed kinetics of the fischer-tropsch synthesis on cobalt catalysts based on H-assisted CO activation”. In: *Topics in Catalysis* 54.13-15 (2011), pp. 786–800. ISSN: 10225528. DOI: 10.1007/s11244-011-9700-3.

[36] Amir Mosayebi and Ali Haghtalab. “The comprehensive kinetic modeling of the Fischer-Tropsch synthesis over Co at Ru/γ-Al2O3 core-shell structure catalyst”. In: *Chemical Engineering Journal* 259 (2015), pp. 191–204. ISSN: 13858947. DOI: 10.1016/j.cej.2014.07.040.

[37] David Vervloet et al. “Fischer-Tropsch reaction-diffusion in a cobalt catalyst particle: aspects of activity and selectivity for a variable chain growth probability”. In: *Catalysis Science & Technology* 2.6 (2012), p. 1221. ISSN: 2044-4753. DOI: 10.1039/c2cy20060k.

[38] Niels G. Deen et al. “Review of direct numerical simulation of fluid-particle mass, momentum and heat transfer in dense gas-solid flows”. In: *Chemical Engineering Science* 116 (2014), pp. 710–724. ISSN: 00092509. DOI: 10.1016/j.ces.2014.05.039.

[39] Ivo A W Filot et al. “Kinetic aspects of chain growth in Fischer-Tropsch synthesis”. In: *Faraday Discussions* 00 (2016), pp. 1–12. ISSN: 1359-6640. DOI: 10.1039/c6fd00205f.

[40] I. A. W. Filot, R. A. van Santen, and E. J. M. Hensen. “Quantum chemistry of the Fischer-Tropsch reaction catalysed by a stepped ruthenium surface”. In: *Catal. Sci. Technol.* 4.9 (2014), pp. 3129–3140. ISSN: 2044-4753. DOI: 10.1039/C4CY00483C.

[41] Ivo A W Filot et al. “First-Principles-Based Microkinetics Simulations of Synthesis Gas Conversion on a Stepped Rhodium Surface”. In: *ACS Catalysis* 5.9 (2015), pp. 5453–5467. ISSN: 21555435. DOI: 10.1021/acscatal.5b01391.

[42] Ferdinand Pöhlmann and Andreas Jess. “Interplay of reaction and pore diffusion during cobalt-catalyzed Fischer - Tropsch synthesis with CO 2 -rich syngas”. In: *Catalysis Today* 275 (2016), pp. 172–182. ISSN: 0920-5861. DOI: 10.1016/j.cattod.2015.09.032.

[43] F. Pöhlmann et al. “Accumulation of liquid hydrocarbons in catalyst pores during cobalt-catalyzed Fischer-Tropsch synthesis”. In: *Catal. Sci. Technol.* 15 (2016), pp. 282–286. ISSN: 2044-4753. DOI: 10.1039/C6CY00941G.

[44] Yi-Ning Wang et al. “Modeling of Catalyst Pellets for Fischer-Tropsch Synthesis”. In: *Industrial & Engineering Chemistry Research* 40.20 (2001), pp. 4324–4335. ISSN: 0888-5885. DOI: 10.1021/ie010080v.

[45] John J. Marano and Gerald D. Holder. “Characterization of Fischer-Tropsch liquids for vapor-liquid equilibria calculations”. In: *Fluid Phase Equilibria* 138.1-2 (1997), pp. 1–21. ISSN: 03783812. DOI: 10.1016/S0378-3812(97)00166-0.

[46] R Krishna and J A Wesselingh. “The Maxwell-Stefan approach to mass transfer”. In: 52.6 (1997), pp. 861–911.

[47] Saurish Das, Niels G. Deen, and J. A. M. Kuipers. “A DNS study of flow and heat transfer through slender fixed-bed reactors randomly packed with spherical particles”. In: *Chemical Engineering Science* 160.October 2016 (2017), pp. 1–19. ISSN: 00092509. DOI: 10.1016/j.ces.2016.11.008.

[48] R. Aris. “On shape factor for irregular particles”. In: *Chemical Engineering Science* 6.1 (1957), pp. 265 –268.

[49] P B Weisz and J S Hicks. “The behavior of porous catalyst particles in view of internal mass and heat diffusion effects”. In: *Chem. Eng. Sci.* 17 (1962), p. 265.

Nomenclature

Greek Symbols

α	Propagation probability	-
β	Adiabatic temperature rise of particle	-
ΔE	Activation energy	$J\ mol^{-1}$
ΔH_r	Reaction enthalpy	$J\ mol^{-1}$
ϵ_b	Bed porosity	$m^3\ m^{-3}$
ϵ_{TP}	Porosity transport pores	-
η	Effectiveness factor	-
γ	Arrhenius number	-
ϕ	Thiele modulus	-
ρ	Density	$kg\ m^{-3}$
τ_{TP}	Tortuosity transport pores	-
ξ	Dimensionless reaction distance	-

Roman Symbols

a	Reaction rate constant	$mol\ s^{-1}\ kg_{cat}^{-1}\ bar^{-2}$
a_p	Specific surface area particle	$m^2\ m^{-3}$
a_R	Specific surface area reactor	$m^2\ m^{-3}$
B	Fitting parameter	-
b	Adsorption constant	bar^{-1}
C	Concentration	$mol\ m^{-3}$
C_p	Specific heat	$J\ kg^{-1}\ K^{-1}$
C_{5+}	Hydrocarbons with carbon number bigger or equal to five	-
D	Diffusion coefficient	$m^2\ s^{-1}$
D^{eff}	Effective diffusion coefficient	$m^2\ s^{-1}$
H_i	Henry coefficient	bar

k	Heat transfer coefficient	$W\ m^{-1}\ K^{-1}$
k'	Reaction rate constant	s^{-1}
k_0	Pre-exponential factor at surface	-
k_α	Fitting parameter	-
N	Amount	-
n	Carbon number	-
p_i	Partial pressure	bar
R	Gas constant	$J\ mol^{-1}\ K^{-1}$
r	Radius	m
R_i	Reaction rate	$mol\ m_{cat}^{-3}\ s^{-1}$
R_p	Propagation rate	$mol\ s^{-1}$
R_t	Termination rate	$mol\ s^{-1}$
S	Selectivity	$kg\ kg^{-1}$
s_E	Source term energy balance	$J\ m^{-3}\ s^{-1}$
s_M	Source term mass balance	$mol\ m^{-3}\ s^{-1}$
STY	Space time yield	$g\ m^{-3}\ s^{-1}$
T	Temperature	K
t	Time	s
U	Bed to wall heat transfer coefficient	$W\ m^{-2}\ K^{-1}$
u	Velocity	$m\ s^{-1}$
V	Volume	m^3
v	Velocity	$m\ s^{-1}$
V_R	Reactor volume	m^3
$V_{GC,i}$	Volume of grid cell i	m^3
W_{AR}	Flux through the catalyst surface	$mol\ m^{-2}\ s^{-1}$
x	Mol fraction	$mol\ mol^{-1}$
Y	Integration variable	-
y	Dimensionless concentration	-

Subscripts

0	Surface of catalyst particle
cat	Catalyst
f	Fluid

i	Specie
n	Carbon number
p	Particle
s	Solid
z	Axial direction in the reactor
CO	Carbon monoxide
H_2O	Water
H_2	Hydrogen

A

Table A.1: H_2 concentration profiles for the 1D particle model, found solving the micro kinetic model for every time step and every grid cell (Solved MKM) and found using a spline for the consumption of H_2. Temperature set to 490 K, surface concentration to 50 mol m^{-3}, pressure 20 bar, syngas ratio to 2 and particle diameter to 3 mm.

	H_2 concentration (mol m^{-3}) at increasing distance from particle center –>																			
Solved MKM	28.58	28.58	28.58	28.59	28.60	28.61	28.62	28.63	28.65	28.67	28.68	28.70	28.72	28.76	28.92	29.67	32.13	36.25	41.34	47.00
Spline	28.79	28.79	28.79	28.80	28.80	28.80	28.80	28.80	28.81	28.81	28.81	28.82	28.82	28.85	28.99	29.72	32.16	36.27	41.35	47.00
Difference %	-0.76	-0.75	-0.74	-0.72	-0.70	-0.67	-0.63	-0.59	-0.55	-0.50	-0.45	-0.40	-0.35	-0.29	-0.23	-0.17	-0.10	-0.05	-0.02	-0.01

Table A.2: Highest temperature rise found via the 1D reactor model in Kelvin.

		H_2/CO = 1					H_2/CO = 2					H_2/CO = 3				
		T = 393.15	T = 443.15	T = 493.15	T = 543.15	T = 593.15	T = 393.15	T = 443.15	T = 493.15	T = 543.15	T = 593.15	T = 393.15	T = 443.15	T = 493.15	T = 543.15	T = 593.15
$C_{H2,in}$ = 10 mol m^{-3}	dp = 5e-4 m	0	0.11	11.59	32.95	42.17	0	0.21	11.36	23.46	30.72	0	0.31	9.19	17.03	22.21
	dp = 2e-3 m	0	0.13	4.32	11.91	16.3	0	0.31	3.74	7.75	10.51	0	0.39	3.02	5.48	7.32
	dp = 5e-3 m	0	0.14	1.79	3.63	4.83	0	0.19	1.37	2.08	2.75	0	0.2	0.97	1.41	1.86
$C_{H2,in}$ = 50 mol m^{-3}	dp = 5e-4 m	0	0.12	210.88	236.97	250.52	0	0.23	166.32	216.99	232.34	0	0.35	111.38	142.7	N/A
	dp = 2e-3 m	0	0.13	27.32	80.69	93.98	0	0.29	29.29	50.22	62.85	0	0.63	22.52	33.85	42.33
	dp = 5e-3 m	0	0.25	7.1	20.57	26.4	0	0.41	7.91	11.11	14.38	0	0.5	5.37	7.43	9.61
$C_{H2,in}$ = 150 mol m^{-3}	dp = 5e-4 m	0	0.12	580.27	674.07	633.87	0	0.24	N/A	N/A	683.67	0	0.36	N/A	N/A	N/A
	dp = 2e-3 m	0	0.13	200.31	224.29	250.3	0	0.28	121.28	N/A	194.7	0	0.45	80.86	106.03	N/A
	dp = 5e-3 m	0	0.37	25.34	64.95	79.3	0	0.68	24.6	33.74	43.5	0	0.94	16.46	22.51	29.02

Table A.3: Selectivities to C_{5+} products in kg/kg

		H2/CO = 1					H2/CO = 2					H2/CO = 3				
		T = 393.15	T = 443.15	T = 493.15	T = 543.15	T = 593.15	T = 393.15	T = 443.15	T = 493.15	T = 543.15	T = 593.15	T = 393.15	T = 443.15	T = 493.15	T = 543.15	T = 593.15
$C_{H2,in}$ = 10 mol m^{-3}	dp = 5e-4 m	0.14	0.64	0.70	0.09	0.01	0.11	0.63	0.69	0.12	0.01	0.11	0.65	0.65	0.11	0.01
	dp = 2e-3 m	0.13	0.64	0.74	0.15	0.02	0.11	0.67	0.71	0.16	0.02	0.11	0.69	0.68	0.13	0.01
	dp = 5e-3 m	0.11	0.66	0.74	0.19	0.02	0.10	0.68	0.70	0.14	0.01	0.10	0.69	0.65	0.10	0.01
$C_{H2,in}$ = 50 mol m^{-3}	dp = 5e-4 m	0.14	0.64	0.17	0.00	0.00	0.11	0.63	0.15	0.00	0.00	0.11	0.65	0.17	0.01	0.00
	dp = 2e-3 m	0.13	0.64	0.58	0.04	0.00	0.11	0.64	0.51	0.06	0.00	0.11	0.68	0.49	0.04	0.00
	dp = 5e-3 m	0.09	0.67	0.70	0.11	0.01	0.09	0.66	0.58	0.06	0.01	0.08	0.64	0.45	0.03	0.00
$C_{H2,in}$ = 150 mol m^{-3}	dp = 5e-4 m	0.14	0.64	0.02	0.00	0.00	0.11	0.63	N/A	N/A	0.00	0.11	0.65	N/A	N/A	N/A
	dp = 2e-3 m	0.13	0.64	0.10	0.01	0.00	0.11	0.64	0.13	N/A	0.00	0.11	0.66	0.13	0.01	N/A
	dp = 5e-3 m	0.08	0.66	0.53	0.03	0.00	0.08	0.66	0.25	0.01	0.00	0.07	0.55	0.13	0.00	0.00

Table A.4: Space time yield of C_{5+} products in $g/m_R^3/s$

		H2/CO = 1					H2/CO = 2					H2/CO = 3				
		T = 393.15	T = 443.15	T = 493.15	T = 543.15	T = 593.15	T = 393.15	T = 443.15	T = 493.15	T = 543.15	T = 593.15	T = 393.15	T = 443.15	T = 493.15	T = 543.15	T = 593.15
$C_{H2,in}$ = 10 mol m^{-3}	dp = 5e-4 m	0.00	1.29	55.13	6.85	0.47	0.00	2.35	50.74	8.47	0.67	0.00	3.40	35.83	5.92	0.53
	dp = 2e-3 m	0.00	1.47	39.34	11.31	1.08	0.00	3.43	32.65	10.33	1.15	0.00	4.45	24.58	6.24	0.65
	dp = 5e-3 m	0.00	1.60	20.02	8.67	1.13	0.00	2.13	14.27	4.18	0.53	0.00	2.23	9.40	2.04	0.22
$C_{H2,in}$ = 50 mol m^{-3}	dp = 5e-4 m	0.00	1.36	24.01	0.43	0.00	0.00	2.59	52.15	2.18	0.00	0.00	3.88	46.80	4.03	N/A
	dp = 2e-3 m	0.00	1.52	148.69	15.00	0.79	0.00	3.12	142.30	19.60	0.93	0.00	6.87	108.85	11.32	0.55
	dp = 5e-3 m	0.00	2.84	74.07	27.49	2.77	0.00	4.44	67.43	9.90	0.99	0.01	5.27	35.14	3.54	0.25
$C_{H2,in}$ = 150 mol m^{-3}	dp = 5e-4 m	0.00	1.37	6.00	0.00	0.00	0.00	2.63	N/A	N/A	0.00	0.00	3.96	N/A	N/A	N/A
	dp = 2e-3 m	0.00	1.53	98.73	11.59	0.23	0.00	3.01	125.81	N/A	0.18	0.00	4.86	94.54	6.72	N/A
	dp = 5e-3 m	0.00	3.98	179.36	24.25	0.84	0.01	7.05	88.33	6.69	0.11	0.01	8.39	31.81	0.80	0.02

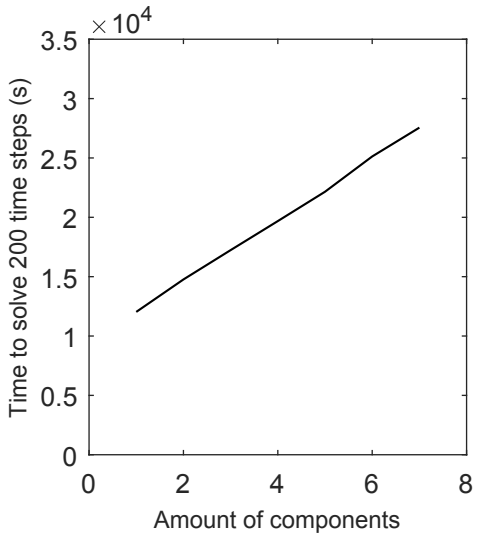

Figure A.1: Computation time for setting 200 time steps for different amounts of species.

Table A.5: Data Aris test case

Grid cells/d_p	Thiele modulus	Efficieny factor IBM	Efficiency factor analytical	Error (%)
20	0.35	0.9940	0.9918	0.22
	0.50	0.9859	0.9837	0.22
	0.71	0.9702	0.9682	0.21
	1.00	0.9409	0.9391	0.19
	1.41	0.8893	0.8878	0.17
	2.00	0.8069	0.8060	0.12
	2.83	0.6934	0.6931	0.047
	4.00	0.5626	0.5630	-0.076
	5.66	0.4353	0.4366	-0.30
	8.00	0.3257	0.3281	-0.73
	11.31	0.2379	0.2417	-1.59
	16.00	0.1701	0.1758	-3.24
40	16.00	0.1736	0.1758	-1.22

Table A.6: Non isothermal reaction diffusion problem data on found effectiveness factors. γ = 20, grids/d_p = 30

β	ϕ	η IBM	η ODE15s	error (%)
0.8	0.3	1.115	1.116	0.11
	0.3	138.051	136.910	-0.83
	0.5	101.144	97.497	-3.74
	1.0	58.966	53.864	-9.47
0.6	0.4	1.162	1.153	-0.78
	0.4	44.943	44.549	-0.88
	0.5	42.473	42.050	-1.00
	1.0	27.959	26.543	-5.33
0.4	0.3	1.049	1.047	-0.12
	0.5	1.161	1.155	-0.51
	1.0	10.200	10.084	-1.15
	2.0	6.629	6.336	-4.62

Table A.7: Global mass balance of H_2 for the flow past a sphere problem. The balance error is the error of the outlet and production compared to the inlet. The flux error is the difference between the production and the flux towards the solid. The mole flows are given in mol per time step.

H2

DHR (kJ/mol)	In (mol/dt)	Out (mol/dt)	Production (mol/dt)	Balance error (%)	Solid Flux (mol/dt)	Flux error (%)
0	8.54E-07	8.01E-07	-5.45E-08	-0.27	-5.40E-08	0.95
5	8.54E-07	7.65E-07	-9.32E-08	-0.50	-9.22E-08	1.07
10	8.54E-07	7.43E-07	-1.25E-07	-1.70	-1.22E-07	2.30
20	8.54E-07	7.29E-07	-1.89E-07	-7.48	-1.75E-07	7.40
40	8.54E-07	7.20E-07	-3.20E-07	-21.85	-2.68E-07	16.12
80	8.54E-07	7.16E-07	-5.22E-07	-45.07	-4.02E-07	23.07
160	8.54E-07	7.15E-07	-7.17E-07	-67.74	-5.11E-07	28.67

Table A.8: Global mass balance of CO for the flow past a sphere problem. The balance error is the error of the outlet and production compared to the inlet. The flux error is the difference between the production and the flux towards the solid. The mole flows are given in mol per time step.

CO

DHR (kJ/mol)	In (mol/dt)	Out (mol/dt)	Production (mol/dt)	Error (%)	Solid Flux (mol/dt)	Error (%)
0	4.27E-07	4.01E-07	-2.69E-08	-0.27	-2.67E-08	0.95
5	4.27E-07	3.83E-07	-4.57E-08	-0.49	-4.52E-08	1.08
10	4.27E-07	3.74E-07	-6.02E-08	-1.6	-5.89E-08	2.30
20	4.27E-07	3.68E-07	-8.74E-08	-6.69	-8.12E-08	7.13
40	4.27E-07	3.66E-07	-1.33E-07	-16.98	-1.14E-07	14.59
80	4.27E-07	3.67E-07	-1.97E-07	-32.09	-1.56E-07	20.80
160	4.27E-07	3.68E-07	-2.61E-07	-47.24	-1.93E-07	25.95

Table A.9: Global mass balance of H_2O for the flow past a sphere problem. The balance error is the error of the outlet and production compared to the inlet. The flux error is the difference between the production and the flux towards the solid. The mole flows are given in mol per time step.

H2O						
DHR (kJ/mol)	In (mol/dt)	Out (mol/dt)	Production (mol/dt)	Error (%)	Solid Flux (mol/dt)	Error (%)
0	0	2.58E-08	2.69E-08	-4.43	2.67E-08	0.95
5	0	4.36E-08	4.57E-08	-4.79	4.52E-08	1.08
10	0	5.33E-08	6.02E-08	-13.13	5.89E-08	2.30
20	0	5.89E-08	8.74E-08	-48.49	8.12E-08	7.13
40	0	6.04E-08	1.33E-07	-119.90	1.14E-07	14.58
80	0	5.97E-08	1.97E-07	-229.26	1.56E-07	20.80
160	0	5.87E-08	2.61E-07	-343.96	1.92E-07	26.41